HAL
open science

Complex organic molecules in strongly UV-irradiated gas

S. Cuadrado, J. Goicoechea, J. Cernicharo, A. Fuente, J. Pety, B. Tercero

To cite this version:

S. Cuadrado, J. Goicoechea, J. Cernicharo, A. Fuente, J. Pety, et al.. Complex organic molecules in strongly UV-irradiated gas. Astronomy and Astrophysics - A&A, 2017, 603, pp.A124. 10.1051/0004-6361/201730459 . hal-02180883

HAL Id: hal-02180883

https://hal.science/hal-02180883

Submitted on 22 Aug 2022

HAL is a multi-disciplinary open access archive for the deposit and dissemination of scientific research documents, whether they are published or not. The documents may come from teaching and research institutions in France or abroad, or from public or private research centers.

L'archive ouverte pluridisciplinaire **HAL**, est destinée au dépôt et à la diffusion de documents scientifiques de niveau recherche, publiés ou non, émanant des établissements d'enseignement et de recherche français ou étrangers, des laboratoires publics ou privés.

A&A 603, A124 (2017)
DOI: 10.1051/0004-6361/201730459
© ESO 2017

Astronomy & Astrophysics

Complex organic molecules in strongly UV-irradiated gas*

S. Cuadrado[1], J. R. Goicoechea[1], J. Cernicharo[1], A. Fuente[2], J. Pety[3,4], and B. Tercero[1]

[1] Grupo de Astrofísica Molecular. Instituto de Ciencia de Materiales de Madrid (CSIC), Sor Juana Inés de la Cruz 3, 28049 Cantoblanco, Madrid, Spain
e-mail: s.cuadrado@icmm.csic.es
[2] Observatorio Astronómico Nacional, Apdo. 112, 28803 Alcalá de Henares, Madrid, Spain
[3] Institut de Radioastronomie Millimétrique (IRAM), 300 rue de la Piscine, 38406 Saint-Martin d'Hères, France
[4] LERMA, Observatoire de Paris, CNRS UMR 8112, École Normale Supérieure, PSL research university, 24 rue Lhomond, 75231 Paris Cedex 05, France

Received 18 January 2017 / Accepted 12 May 2017

ABSTRACT

We investigate the presence of complex organic molecules (COMs) in strongly UV-irradiated interstellar molecular gas. We have carried out a complete millimetre (mm) line survey using the IRAM 30 m telescope towards the edge of the Orion Bar photodissociation region (PDR), close to the H_2 dissociation front, a position irradiated by a very intense far-UV (FUV) radiation field. These observations have been complemented with 8.5″ resolution maps of the H_2CO $J_{K_a,K_c} = 5_{1,5} \rightarrow 4_{1,4}$ and $C^{18}O$ $J = 3 \rightarrow 2$ emission at 0.9 mm. Despite being a harsh environment, we detect more than 250 lines from COMs and related precursors: H_2CO, CH_3OH, HCO, H_2CCO, CH_3CHO, H_2CS, HCOOH, CH_3CN, CH_2NH, HNCO, $H_2^{13}CO$, and HC_3N (in decreasing order of abundance). For each species, the large number of detected lines allowed us to accurately constrain their rotational temperatures (T_{rot}) and column densities (N). Owing to subthermal excitation and intricate spectroscopy of some COMs (symmetric- and asymmetric-top molecules such as CH_3CN and H_2CO, respectively), a correct determination of N and T_{rot} requires building rotational population diagrams of their rotational ladders separately. The inferred column densities are in the 10^{11}–10^{13} cm^{-2} range. We also provide accurate upper limit abundances for chemically related molecules that might have been expected, but are not conclusively detected at the edge of the PDR (HDCO, CH_3O, CH_3NC, CH_3CCH, CH_3OCH_3, $HCOOCH_3$, CH_3CH_2OH, CH_3CH_2CN, and CH_2CHCN). A non-thermodynamic equilibrium excitation analysis for molecules with known collisional rate coefficients suggests that some COMs arise from different PDR layers but we cannot resolve them spatially. In particular, H_2CO and CH_3CN survive in the extended gas directly exposed to the strong FUV flux (T_k = 150–250 K and $T_d \gtrsim 60$ K), whereas CH_3OH only arises from denser and cooler gas clumps in the more shielded PDR interior (T_k = 40–50 K). The non-detection of HDCO towards the PDR edge is consistent with the minor role of pure gas-phase deuteration at very high temperatures. We find a $HCO/H_2CO/CH_3OH \simeq 1/5/3$ abundance ratio. These ratios are different from those inferred in hot cores and shocks. Taking into account the elevated gas and dust temperatures at the edge of the Bar (mostly mantle-free grains), we suggest the following scenarios for the formation of COMs: (i) hot gas-phase reactions not included in current models; (ii) warm grain-surface chemistry; or (iii) the PDR dynamics is such that COMs or precursors formed in cold icy grains deeper inside the molecular cloud desorb and advect into the PDR.

Key words. astrochemistry – surveys – photon-dominated region (PDR) – ISM: molecules – ISM: abundances

1. Introduction

Almost 200 molecules have been detected in the interstellar medium (ISM) and circumstellar shells. A very large fraction of them are complex organic molecules (COMs). COMs are traditionally defined as carbon-based molecular species with more than six atoms in their structure (Herbst & van Dishoeck 2009; Caselli & Ceccarelli 2012). To date, the largest organic molecules detected in the ISM (excluding PAHs and fullerenes) are propyl cyanide (C_3H_7CN; Belloche et al. 2009, 2014) and benzene (c-C_6H_6; Cernicharo et al. 2001).

COMs have been detected in the ISM since the 1970s (e.g. CH_3CHO, Gottlieb 1973; or $HCOOCH_3$, Brown et al. 1975). Most of the detections have been reported towards hot cores, that is, dense gas surrounding high-mass protostars in massive star-forming regions such as Sgr B2 and Orion KL (e.g. Bisschop et al. 2007; Ziurys & McGonagle 1993; Tercero et al. 2013, 2015; Ikeda et al. 2001), and towards hot corinos, that is, the low-mass analogs of hot cores such as IRAS 16293-2422 (Cazaux et al. 2003) and NGC 1333 IRAS 4A (Bottinelli et al. 2004). The high degree of chemical complexity (e.g. C_2H_5CN, CH_3CCH, $HCOOCH_3$, CH_3OCH_3, ...) found in these protostellar sources is thought to result from thermal desorption of the ice mantles coating dust grains. Herbst & van Dishoeck (2009) have reviewed the subject. They classify the observed COMs towards protostars in three different generations depending on the time they are produced. The zeroth-generation species, such as H_2CO and CH_3OH, are formed through grain-surface reactions in a previous cold interstellar phase in which icy mantles built up around granular cores of carbon and silicate grains. The first-generation species, such as $HCOOCH_3$, are formed during the passive warm-up of the inner envelope of the protostar. During this phase, zeroth-generation species are photodissociated producing radicals such as HCO and CH_3O, which can associate through surface reactions to form larger molecules. Finally, the

* Based on observations obtained with the IRAM 30 m telescope. IRAM is supported by INSU/CNRS (France), MPG (Germany), and IGN (Spain).

second-generation species are formed once the core has become a hot core or hot corino. The dust temperature at this stage is high enough ($T_d \gtrsim 100$ K) to sublimate the mantles completely, and new molecules are formed through warm gas-phase reactions (ion molecule and endothermic neutral-neutral reactions).

When protostellar outflows impact the ambient envelope material, grains can be eroded, and because of the high temperatures reached in shocks, icy mantles can sublimate. In sufficiently high-velocity shocks, ices can also be sputtered and directly injected into the gas phase (e.g. $v_s > 20-25$ km s^{-1} for water ice, Draine et al. 1983). Several observations of the L1157 outflow have revealed the existence of H_2CO, H_2CS, CH_3OH, HC_3N, HNCO, NH_2CHO, and CH_3CHO in shocked gas (Bachiller & Pérez Gutiérrez 1997; Mendoza et al. 2014; Codella et al. 2015). In addition, Requena-Torres et al. (2006) have shown that the galactic centre contains dense clouds that are rich in CH_3OH, $HCOOCH_3$, and CH_3OCH_3. Widespread shocks have been invoked to explain their abundance and extended spatial distribution. The relative importance of the gas-phase reactions immediately after ice mantle sublimation compared to a formation of COMs on the grain surfaces is however far from being understood.

Recent observations towards UV-shielded cold cores (e.g. TMC 1, L1689B, or Barnard 1-b) have revealed molecules once considered to be present only in hot molecular cores (e.g. Remijan et al. 2006; Bacmann et al. 2012; Cernicharo et al. 2012). In these cold environments, COMs are thought to form on the surface of grains and to be released through non-thermal desorption processes, chemical desorption, direct desorption by cosmic ray impacts, or secondary photon induced processes (Cernicharo et al. 2012). Finally, a number of organic species have been identified in circumstellar envelopes around evolved stars (e.g. IRC+10216, Cernicharo et al. 2000), towards extragalactic sources (e.g. Meier & Turner 2005, 2012; Aladro et al. 2011), meteorites (e.g. Cronin & Chang 1993), and comets (e.g. Bockelée-Morvan et al. 2004).

Studies of environments permeated by stellar far-UV (FUV) photons (6.0 eV < $h\nu$ < 13.6 eV) are more scarce. Guzmán et al. (2014) and Gratier et al. (2013) presented the unexpected detection of HCOOH, CH_2CO, CH_3CN, CH_3OH, CH_3CHO, and CH_3CCH in the Horsehead photodissociation region (PDR; a relatively low-FUV-flux dense PDR, $\chi \approx 60$ times the mean interstellar field in Draine units), finding enhanced abundances compared to a nearby cold and dense core shielded from external FUV radiation. Guzmán et al. (2014) proposed that owing to the cold grain temperatures, ice-mantle photodesorption processes dominate the formation of COMs in the Horsehead. In lower-density translucent clouds ($\chi \approx 1$), only H_2CO has been unambiguously detected (Liszt et al. 2006). These observations might suggest that, in FUV-irradiated environments, the presence of COMs diminishes as the χ/n_H ratio increases. Thus, COMs might not be present in strongly FUV-irradiated gas.

In this work we test the above hypothesis and investigate the presence and abundances of COMs at the high FUV-illuminated edge of the Orion Bar, with an impinging radiation field of a few 10^4 times the mean interstellar field (Marconi et al. 1998). Because of its proximity (414 ± 7 pc, Menten et al. 2007) and nearly edge-on orientation, the Orion Bar provides an excellent template to determine the chemical content and also to investigate the structure and dynamics of strongly FUV-irradiated molecular gas (e.g. Tielens et al. 1993; Hogerheijde et al. 1995; Cuadrado et al. 2015, 2016; Goicoechea et al. 2016).

Multi-wavelength observations towards different positions of the Orion Bar have been historically used in the development of PDR models (e.g. Tielens & Hollenbach 1985a,b) and today they are still used as a template to understand the unresolved emission from sources as different as the nuclei of distant starburst galaxies (e.g. Fuente et al. 2008) or the illuminated surfaces of protoplanetary disks (e.g. Agúndez et al. 2008). The transition from ionised to neutral gas in the Orion Bar has been extensively mapped, generally at low angular resolution, in various atomic and molecular tracers (see e.g. Tielens et al. 1993; Hogerheijde et al. 1995; van der Werf et al. 1996; Walmsley et al. 2000; Leurini et al. 2010; Ossenkopf et al. 2013). The detailed analysis of these observations suggested an inhomogeneous density distribution. The most commonly accepted scenario is that an extended gas component, with mean gas densities of 10^4–10^5 cm^{-3}, causes the chemical stratification seen perpendicular to the dissociation front as the FUV field is attenuated (Hogerheijde et al. 1995; Jansen et al. 1995; Simon et al. 1997; van der Wiel et al. 2009; Habart et al. 2010; van der Tak et al. 2013). In addition, another component of clumpy material with higher densities ($\gtrsim 10^6$ cm^{-3}) and more shielded from FUV radiation is embedded in the interclump gas (Burton et al. 1990; Parmar et al. 1991; Stoerzer et al. 1995; Young Owl et al. 2000; Lis & Schilke 2003; Batrla & Wilson 2003; Andree-Labsch et al. 2017). Previous observations of H_2CO and CH_3OH in the Orion Bar have shown that the two molecules trace these two different environments: CH_3OH, the denser and cooler clumps seen deeper inside the Bar, and H_2CO, the warmer interclump medium directly exposed to the strong FUV-field (Leurini et al. 2006, 2010).

We have performed a complete millimetre line survey using the IRAM 30 m telescope towards the edge of Orion Bar, a high FUV-illuminated position close to what Stoerzer et al. (1995) call the "CO^+ peak", near the H_2 dissociation front (see Fig. 1). This position shows a distinctive chemistry that can only be understood due to the presence of a strong flux of FUV photons (e.g. compared to that in the more shielded clumps deeper inside the Bar): enhanced abundances of simple reactive ions (e.g. CH^+, CO^+, and HOC^+) and small hydrocarbon ions (e.g. l-C_3H^+) that are only abundant in the presence of C^+; vibrationally excited H_2; and high gas temperatures (e.g. Nagy et al. 2013; Guzmán et al. 2015; Cuadrado et al. 2015). Indeed, high-angular resolution ALMA-ACA images do show that reactive ions such as SH^+ or HOC^+ do not emit from the more shielded clumps (Goicoechea et al. 2017). Therefore, their chemistry is different to that of the PDR edge observed in this work. Our survey covers ~220 GHz of bandwidth, between 80 GHz and 360 GHz. These observations have been complemented with several 8.5″ resolution maps of different molecules at 0.9 mm to put our line survey position in the context of the Bar large-scale emission. In this paper we focus on the detection of rotational lines from COMs and related precursors.

The paper is organised as follows. In Sect. 2 we describe the line survey and the mapping observations. In Sect. 3 we report the observational features of the detected organic molecules, while in Sect. 4 we present the $C^{18}O$ and H_2CO integrated line intensity maps at 0.9 mm. The data analysis is explained in Sect. 5. In Sect. 6 we discuss the results, and finally in Sect. 7 we summarise the main conclusions.

2. Observations and data reduction

2.1. Line survey

We performed a complete millimetre line survey towards the edge of Orion Bar using the IRAM 30 m telescope. The target position is at $\alpha_{2000} = 05^h\,35^m\,20.8^s$,

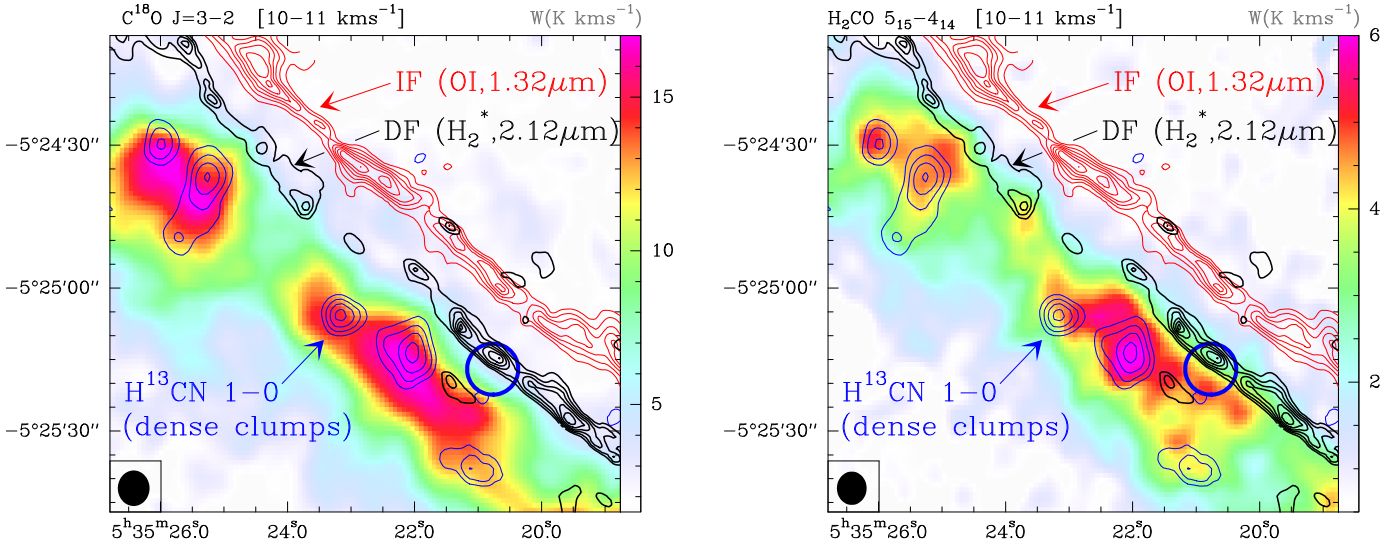

Fig. 1. $C^{18}O$ $J = 3 \rightarrow 2$ (*left panel*) and H_2CO $J_{K_a,K_c} = 5_{1,5} \rightarrow 4_{1,4}$ (*right panel*) line integrated intensity maps (W in K km s^{-1}) in the 10−11 km s^{-1} velocity interval observed with the IRAM 30 m telescope at ~329 GHz and ~351 GHz, respectively (colour scale). Black contours are the H_2^* $v = 1 \rightarrow 0$ $S(1)$ emission delineating the H_2 dissociation front (DF, Walmsley et al. 2000). The red contours represent the O I fluorescent line at 1.32 μm (Walmsley et al. 2000) marking the position of the ionisation front (IF) that separates the H II region and the neutral cloud. The blue contours represent the $H^{13}CN$ $J = 1 \rightarrow 0$ emission tracing dense molecular clumps inside the Bar (Lis & Schilke 2003). The target position of the Orion Bar survey, close to the DF, is indicated with a blue circle. The IRAM 30 m beam at 1 mm is plotted in the bottom left corner (black circle).

Table 1. Observed frequency ranges and telescope parameters.

Rec.[a]	Backend	Freq.[b] [GHz]	δv[c] [km s^{-1}]	η_{MB}[d]	HPBW[e] [arcsec]
E0	FFTS	80−117	0.75−0.51	0.87−0.82	31−21
E1	WILMA	128−176	4.7−3.4	0.80−0.74	19−14
E2	FFTS	202−275	0.30−0.22	0.70−0.56	12−9
E3	FFTS	275−305	0.22−0.20	0.56−0.50	9−8
	FFTS	328−359	0.18−0.17	0.46−0.40	8−7

Notes. [(a)] Emir receiver. [(b)] Observed frequency range. [(c)] Spectral resolution in velocity units (δv) in the observed frequency ranges. [(d)] Antenna efficiencies. [(e)] The half power beam width can be well fitted by HPBW[arcsec] ≈ 2460/Frequency[GHz].

$\delta_{2000} = -05°25'17.0''$, close to the dissociation front. This position is at $(\Delta\alpha, \Delta\delta) = (3'', -3'')$ from the "CO^+ peak" of Stoerzer et al. (1995).

Our observations cover a total of 217 GHz along 3, 2, 1, and 0.9 mm bands of the EMIR receivers using the WILMA (2 MHz spectral resolution) and FTS (200 kHz spectral resolution) backends. The observing procedure was position switching (PSW) with the reference position located at an offset (−600″, 0″) to avoid the extended molecular emission from the Orion Molecular Cloud (OMC-1). The antenna temperature, T_A^*, was converted to the main beam temperature, T_{MB}, through the $T_{MB} = T_A^*/\eta_{MB}$ relation, where η_{MB} is the antenna efficiency. All intensities in tables and figures are in main beam temperature. A local standard of rest (LSR) of 10.7 km s^{-1} has been used in the line survey target position in the Orion Bar dissociation front. Table 1 shows an overview of the frequency ranges observed with each backend, the spectral resolution in velocity units (δv) in the observed frequency ranges, as well as the variation in the telescope efficiencies, η_{MB}, and the half power beam width (HPBW) across the covered frequency range.

In Appendix A we study the possible contamination of bright molecular line emission from the Orion BN/KL region (located at a distance of ~2′) through the beam side lobes (several arcmin, see Greve et al. 1998). Although the contribution to the detected power ranges from ~12% (3 mm) to ~30% (0.8 mm), most of the emission from the hot core region arises at different velocities (~8 km s^{-1}) than those of the Orion Bar (~10−11 km s^{-1}) and thus can be easily separated.

Data reduction and spectral analysis were done using the CLASS software of the GILDAS package[1] developed by IRAM. Weighted spectra were averaged and calibrated, and a polynomial baseline of low order (typically second or third order) was subtracted from each ~200 MHz wide spectrum. Finally, Gaussian profiles were fitted to all the detected lines (Appendix B). The rms noise of our observations obtained after integration during ~4 h ranges between 4 mK and 20 mK per resolution channel.

2.2. Maps

The 0.9 mm line emission from different molecules was mapped with the IRAM 30 m telescope in January 2014 under excellent winter conditions (<1 mm of precipitable water vapour). The E3 receiver and the FTS backend at 200 kHz spectral resolution were used. On-the-fly (OTF) scans were obtained along and perpendicular to the Bar over a 170″ × 170″ region, with an OFF position at (−600″, 0″) relative to the map centre at $\alpha_{2000} = 05^h\,35^m\,20.1^s$, $\delta_{2000} = -05°25'07.0''$, which is slightly different from that of the line survey (see above). The HPBW at this frequency is ~7″. Data processing consisted in a linear baseline subtraction in each observed spectra. The resulting spectra were gridded to a data cube through convolution with a Gaussian kernel providing a final resolution of 8.5″. The total integration

[1] http://www.iram.fr/IRAMFR/GILDAS/

Table 2. Dipole moments (μ), number of detected lines of complex organic molecules and related organic precursors, and their corresponding Figure and Table numbers.

Molecule	No. of lines	μ [Debyes]		Fig.	Table
HCO	16	$\mu_a = 1.363$	$\mu_b = 0.700^a$	2	B.1
H_2CO	15	$\mu_a = 2.332^b$		3	B.2
$H_2^{13}CO$	8	$\mu_a = 2.332^b$		4	B.3
H_2CS	26	$\mu_a = 1.649^b$		5	B.4
HNCO	6	$\mu_a = 1.602$	$\mu_b = 1.350^c$	6	B.5
CH_2NH	6	$\mu_a = 1.340$	$\mu_b = 1.446^d$	7	B.6
H_2CCO	30	$\mu_a = 1.422^b$		8	B.7
HC_3N	11	$\mu_a = 3.732^e$		9	B.8
CH_3CN	44	$\mu_a = 3.922^f$		11	B.9
CH_3OH	55	$\mu_a = 0.896$	$\mu_b = 1.412^g$	12	B.10
CH_3CHO	36	$\mu_a = 2.423$	$\mu_b = 1.260^h$	13	B.11

References. [(a)] Blake et al. (1984); [(b)] Fabricant et al. (1977); [(c)] Hocking et al. (1975); [(d)] Allegrini et al. (1979); [(e)] DeLeon & Muenter (1985); [(f)] Gadhi et al. (1995); [(g)] Sastry et al. (1981); [(h)] Kleiner et al. (1996).

time was approximately 6 h, and the achieved rms noise is ~1 K per ~0.2 km s^{-1} channel. Figure 1 shows the $C^{18}O$ $J = 3 \rightarrow 2$ and H_2CO $J_{K_a,K_c} = 5_{1,5} \rightarrow 4_{1,4}$ integrated line intensity maps in the range $v_{LSR} = 10-11$ km s^{-1} in which the Orion Bar shows prominent emission. We note that van der Wiel et al. (2009) also presented a smaller H_2CO $J_{K_a,K_c} = 5_{1,5} \rightarrow 4_{1,4}$ map at lower angular resolution (a factor of ~2 lower).

3. Results: complex organic molecule detections

We have identified more than 250 lines from COMs and related organic precursors. The detected lines are attributed to ten different molecules with up to seven atoms: HCO, HNCO, H_2CO, H_2CS, CH_2NH, H_2CCO, HC_3N, CH_3OH, CH_3CN, and CH_3CHO. We also detect several lines of the isotopologue $H_2^{13}CO$. We note that among the organic molecules, we also identified several lines of formic acid, trans- and cis-HCOOH, in the Orion Bar PDR. Cuadrado et al. (2016) have recently reported the first detection of the cis conformer of HCOOH in the interstellar medium as well as a detailed analysis of the detected lines of both HCOOH conformers in the 3 mm spectral band. Line profiles peak at $v_{LSR} = 10-11$ km s^{-1}, the velocity of the Bar, thus confirming their PDR origin. The detected organic molecules and their dipole moments are listed in Table 2.

Previous studies of the Orion Bar have already reported the presence of HCO, H_2CO, and CH_3OH in several positions close to the "CO^+ peak": (i) Schilke et al. (2001) detected one hyperfine component of HCO $N = 1 \rightarrow 0$ using the IRAM 30 m telescope; (ii) Hogerheijde et al. (1995) detected nine lines of H_2CO and three lines of CH_3OH in several positions along the Bar using the JCMT, IRAM 30 m, and CSO telescopes; (iii) Nagy et al. (2017) detected ten submm H_2CO lines with *Herschel*/HIFI. In addition, H_2CO, $H_2^{13}CO$, HDCO, H_2CS, and CH_3OH have been detected towards the colder, denser, and more FUV-shielded clumps: (iv) Leurini et al. (2006) detected seven lines of H_2CO, four lines of H_2CS, and ten lines of CH_3OH using APEX between 279 GHz and 361.5 GHz towards clump #1 of Lis & Schilke (2003); (v) Parise et al. (2009) also detected two isotopologues, one line of $H_2^{13}CO$ and one line of HDCO, towards clump #3 of Lis & Schilke (2003) using the IRAM 30 m telescope. To our knowledge, our work presents the first detection of CH_2NH, H_2CCO, HC_3N, CH_3CN, and CH_3CHO in the Orion Bar PDR.

Line assignment was carried out using J. Cernicharo's spectral catalogue (MADEX, Cernicharo 2012), and the JPL (Pickett et al. 1998)[2] and CDMS (Müller et al. 2001, 2005)[3] public databases. Although some lines have peak intensities lower than 3σ noise level, we included them in our results as tentative detections because other transitions from the same molecule are well detected in this survey, and these 3σ limits are in agreement with our excitation models. Given their intricate spectroscopy, below we summarise the main spectroscopic information of the detected species.

3.1. Formyl radical: HCO

The formyl radical, HCO, is a light asymmetric rotor with one unpaired electron and one non-zero nuclear spin. The quantum numbers designating the energy levels are N, J, and F. Spin doubling ($J = N + S$) is produced by the coupling between the rotational angular momentum, N, and the unpaired electron spin, S, while the hyperfine structure ($F = J + I$) is due to the coupling of the angular momentum, J, and the spin of the hydrogen nucleus, I. Each rotational level N_{K_a,K_c} is split into a doublet by the spin-rotation interaction, the levels of which are further split into doublets by magnetic hyperfine interactions, with the final energy levels labelled by the quantum number $F = J \pm 1/2$ (e.g. Bowater et al. 1971; Saito 1972; Austin et al. 1974; Blake et al. 1984). a-type ($\Delta K_a = 0, \pm 2, ...$) and b-type ($\Delta K_a = \pm 1, \pm 3, ...$) transitions are allowed, with a stronger dipole moment for the a-type transitions (see Table 2).

We identified a total of 16 lines of HCO. They consist of four sets of rotational transitions corresponding to the hyperfine splitting of the $N = 1 \rightarrow 0$ to $4 \rightarrow 3$ transitions. All transitions observed here are a-type. The quantum numbers of the detected HCO transitions, their spectroscopic parameters, and the results from fitting the line profiles with Gaussians are listed in Table B.1. In Fig. 2 we present the spectra of the $N = 1 \rightarrow 0$ to $4 \rightarrow 3$ rotational lines.

3.2. Formaldehyde: H_2CO

Formaldehyde, H_2CO, was the first polyatomic organic molecule found in the ISM (Snyder et al. 1969). It is a slightly asymmetric prolate rotor molecule with K-type doublets and an ortho-para symmetry because of the two indiscernible off-axis hydrogen atoms. The ortho states are those with K_a odd, and the para states with K_a even. The nuclear spin weights are 3 and 1 for o-H_2CO and p-H_2CO, respectively. The K-type doublets are the result of the slight asymmetry in the H_2CO produced by the light H atoms. There are no line doublets in the $K_a = 0$ para state (e.g. Bocquet et al. 1996; Brünken et al. 2003; Eliet et al. 2012).

We detected nine lines of the ortho species (in the $K_a = 1$ and 3 ladders) with $E_u/k \leq 125.8$ K, and six lines for the para species (in the $K_a = 0$ and 2 ladders) with $E_u/k \leq 82.1$ K. Line profiles are shown in Fig. 3. Table B.2 gives the observed line parameters.

We also detected eight lines of $H_2^{13}CO$, consisting of six lines of ortho species and two lines of the para species, in the $K_a = 0$

[2] http://spec.jpl.nasa.gov/
[3] http://www.astro.uni-koeln.de/cdms/

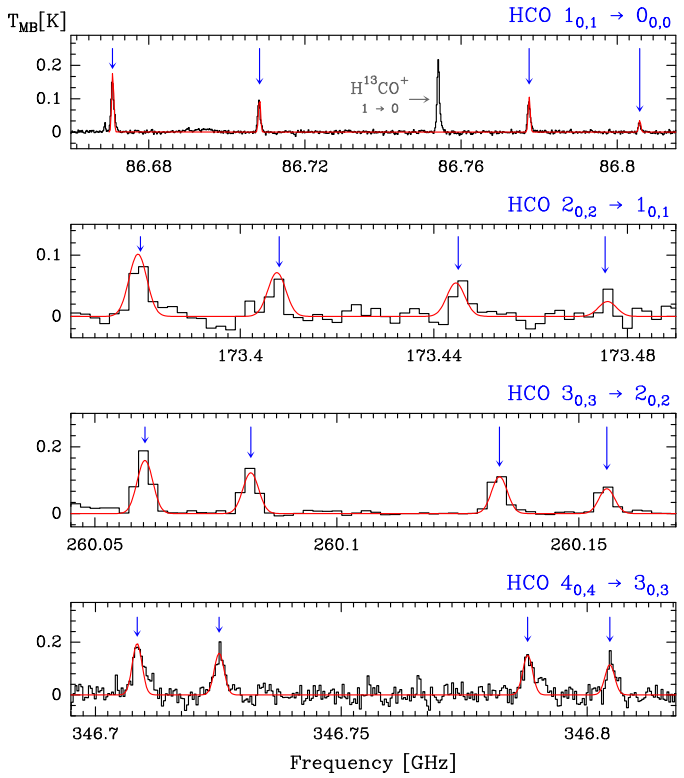

Fig. 2. Detected HCO hyperfine structure (HFS) lines of the $N = 1 \rightarrow 0$, $2 \rightarrow 1$, $3 \rightarrow 2$, and $4 \rightarrow 3$ rotational transitions (black histogram spectra). A single excitation temperature model is shown overlaid in red (see Sect. 5.4). HFS lines are indicated by the blue arrows. The other spectral features appearing in the selected windows are labelled with their corresponding identification.

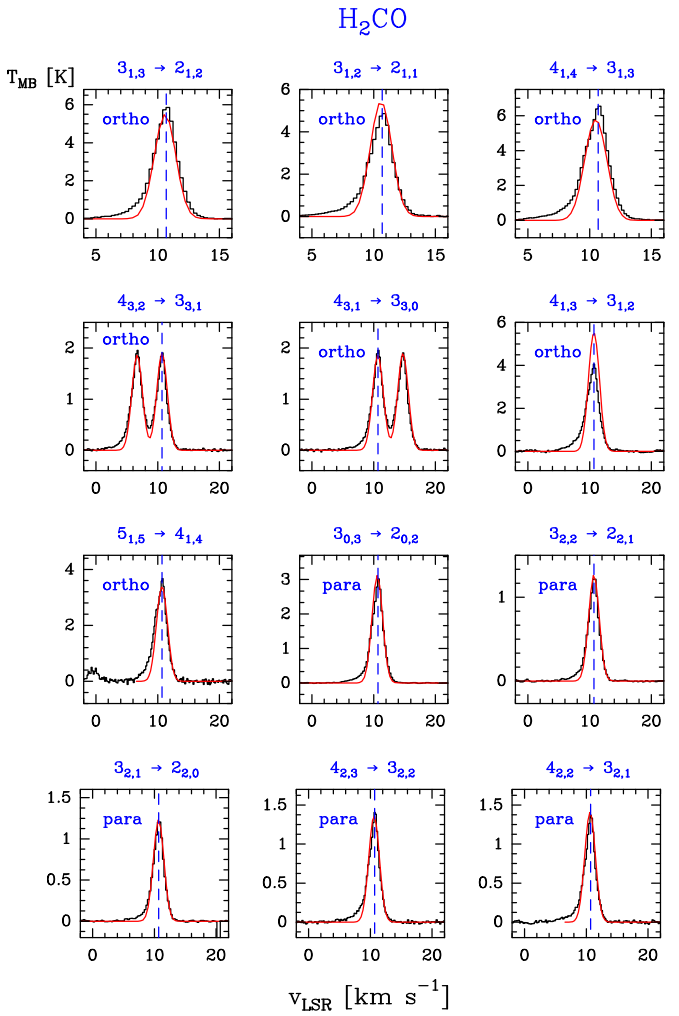

Fig. 3. Example of ortho- and para-H_2CO lines (black histogram spectra). A non-LTE LVG model ($T_k \simeq 200$ K, $n(H_2) \simeq 1 \times 10^6$ cm^{-3}, N(o-H_2CO) = 4.0×10^{13} cm^{-2}, and N(p-H_2CO) = 1.8×10^{13} cm^{-2}) is shown overlaid in red (see Sect. 5.2). The dashed lines indicate the LSR velocity (10.7 km s^{-1}) of the Orion Bar PDR.

and 1 ladders, respectively ($E_u/k \leq 34.0$ K). Line profiles are shown in Fig. 4. Table B.3 gives the observed line parameters. No lines of deuterated formaldehyde were detected.

3.3. Thioformaldehyde: H_2CS

Thioformaldehyde, H_2CS, has a formaldehyde-like structure. It is a slightly asymmetric prolate rotor, with only *a*-type transitions and ortho-para symmetry (e.g. Johnson et al. 1971; Beers et al. 1972; Maeda et al. 2008).

We detected 15 lines of ortho species (in the $K_a = 1$ and 3 ladders) with $E_u/k \leq 149.8$ K, and 11 lines of para species (in the $K_a = 0$ and 2 ladders) with $E_u/k \leq 112.0$ K. Figure 5 shows a selection of ortho and para detected lines. Table B.4 gives the observed line parameters.

3.4. Isocyanic acid: HNCO

Isocyanic acid, H-N=C=O, is the simplest molecule containing carbon, hydrogen, oxygen, and nitrogen. It is a slightly asymmetric prolate rotor with *a*- and *b*-type transitions. Its rotational levels are designated as J_{K_a,K_c} (e.g. Kukolich et al. 1971; Hocking et al. 1975; Lapinov et al. 2007).

We detect six *a*-type transitions inside the $K_a = 0$ rotational ladder ($E_u/k \leq 96.0$ K). The observed lines do not show evidence for hyperfine splittings. Line profiles are shown in Fig. 6. Table B.5 gives the observed line parameters.

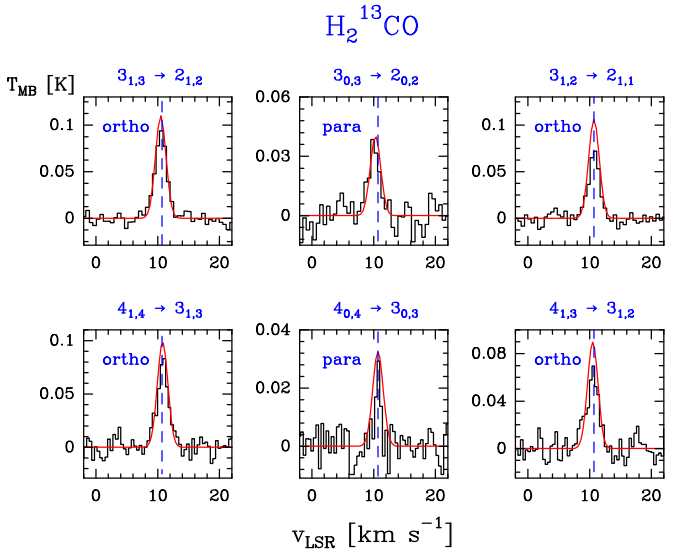

Fig. 4. Example of ortho- and para-$H_2^{13}CO$ lines (black histogram spectra). A non-LTE LVG model ($T_k \simeq 200$ K, $n(H_2) \simeq 1 \times 10^6$ cm^{-3}, N(o-$H_2^{13}CO$) = 7.3×10^{11} cm^{-2}, and N(p-$H_2^{13}CO$) = 2.3×10^{11} cm^{-2}) is shown overlaid in red (see Sect. 5.2).

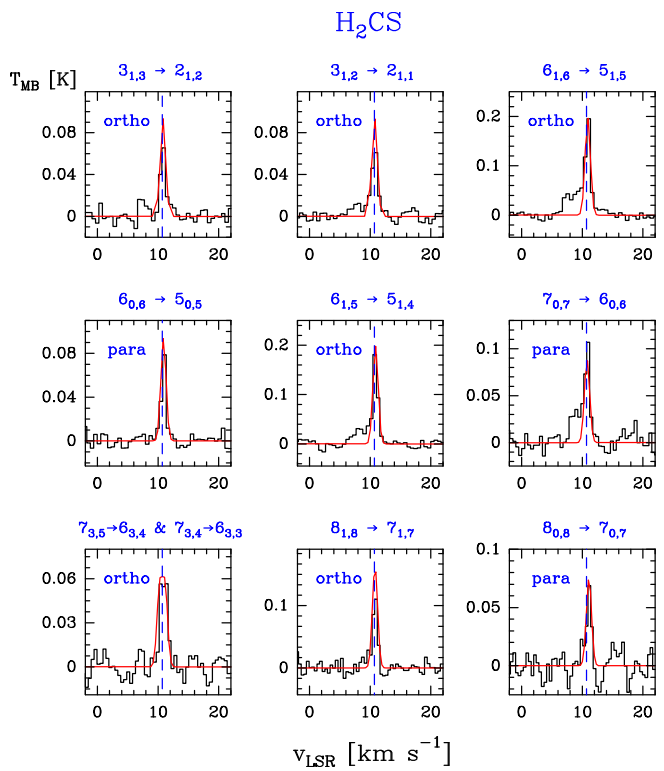

Fig. 5. Example of ortho- and para-H_2CS lines (black histogram spectra). Single excitation temperature models are shown overlaid in red (see Sect. 5.4).

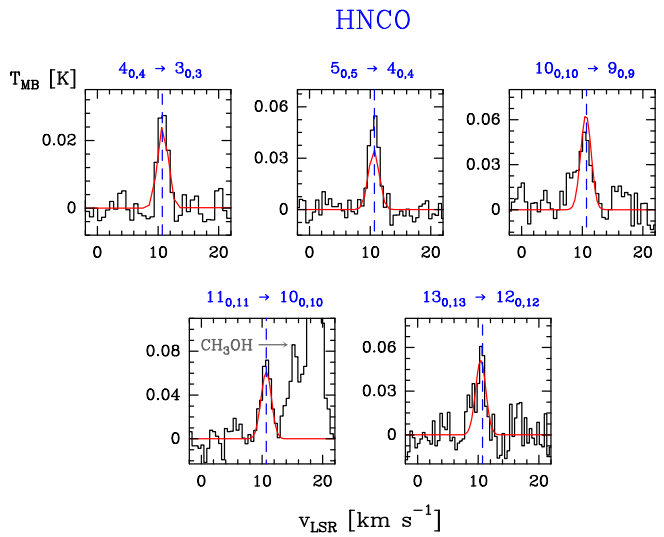

Fig. 6. Example of HNCO detected lines (black histogram spectra). A single excitation temperature model is shown overlaid in red (see Sect. 5.4).

3.5. Methanimine: CH_2NH

Methanimine is the simplest molecule containing a carbon-nitrogen double bond ($H_2C{=}NH$). It is a planar molecule and a nearly prolate asymmetric rotor with components of the electric dipole moment along both the a and b molecular axes (e.g. Kirchhoff et al. 1973; Dore et al. 2010, 2012).

We detected six lines of CH_2NH consisting of (i) three a-type transitions (in the $K_a = 0$ and 1 ladders) and (ii) three b-type transitions, with $E_u/k \leq 64.1$ K. The observed lines do not show evidence for hyperfine splittings. The line profiles are shown in Fig. 7. Table B.6 gives the observed line parameters.

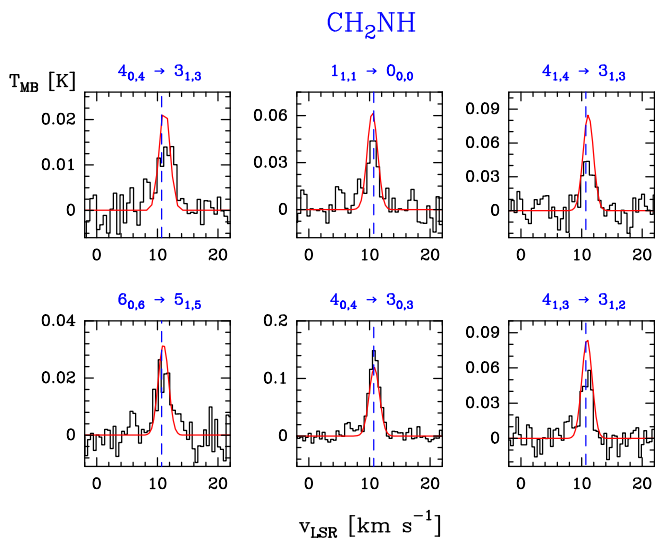

Fig. 7. CH_2NH detected lines (black histogram spectra). A single excitation temperature model is shown overlaid in red (see Sect. 5.4).

3.6. Ketene: H_2CCO

Ketene, $H_2C{=}C{=}O$, is a slightly asymmetric prolate rotor with only a-type transitions and ortho-para symmetry (e.g. Johnson & Strandberg 1952; Fabricant et al. 1977; Brown et al. 1990; Johns et al. 1992). We detected 20 lines of ortho species (in the $K_a = 1$ and 3 ladders) with $E_u/k \leq 205.2$ K, and ten lines for the para species (in the $K_a = 0$ and 2 ladders) with $E_u/k \leq 154$ K. Examples of the line profiles of ortho and para lines are shown in Fig. 8. Table B.7 gives the observed line parameters.

3.7. Cyanoacetylene: HC_3N

Cyanoacetylene, H–C≡C–C≡N, is a linear molecule with a large dipole moment of $\mu_a = 3.732$ D (DeLeon & Muenter 1985). It is the simplest example of cyanopolyynes, HC_nN (with $n = 3$, 5, 7, ...; see e.g. Turner 1971; Avery et al. 1976; Cernicharo et al. 1986). The rotational transitions show hyperfine splittings owing to the interaction of the electric-quadrupole moment of the nitrogen nuclear spin with the electronic-charge distribution (e.g. de Zafra 1971; Mbosei et al. 2000; Chen et al. 1991; Yamada et al. 1995; Thorwirth et al. 2000). This hyperfine splitting is only fully resolved in the lowest rotational transitions (e.g. Turner 1971; Dickinson 1972), therefore, HC_3N is described here by a simple rotational spectrum, with $J{+}1 \rightarrow J$ transitions.

We detected 11 lines of HC_3N, from $J = 9 \rightarrow 8$ to $24 \rightarrow 23$, with $E_u/k \leq 131.0$ K. Figure 9 shows a selection of detected lines and Table B.8 gives the observed line parameters.

3.8. Methyl cyanide: CH_3CN

Methyl cyanide, CH_3CN, is a strongly prolate symmetric rotor, therefore, the permitted radiative transitions are all $\Delta K = 0$. The internal rotation of the methyl group gives rise to two non-interacting torsional substates, denoted A and E. The A state levels are described by $K = 3n$, and those of E state by

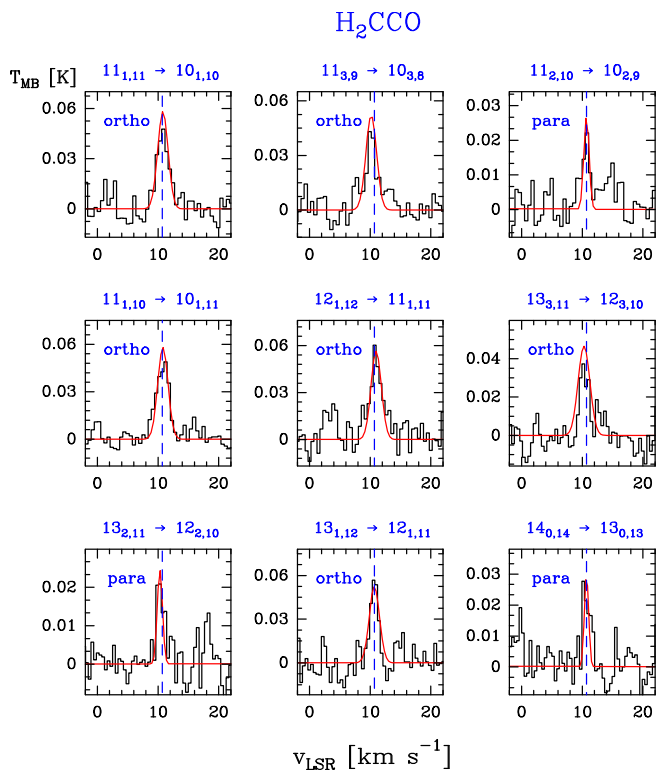

Fig. 8. Example of ortho- and para-H_2CCO lines (black histogram spectra). Single excitation temperature models are shown overlaid in red (see Sect. 5.4).

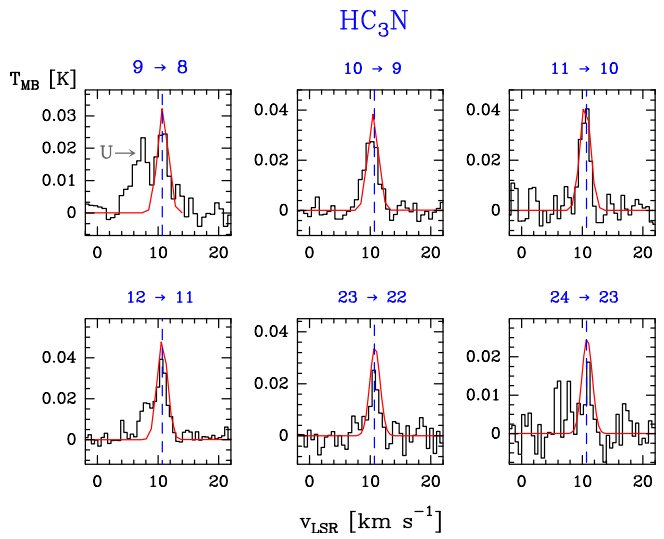

Fig. 9. Example of HC_3N detected lines (black histogram spectra). A non-LTE LVG model ($T_k \simeq 80$ K, $n(H_2) \simeq 1 \times 10^6$ cm^{-3}, $N(HC_3N) = 4.0 \times 10^{11}$ cm^{-2}) is shown overlaid in red (see Sect. 5.2).

$K = 3n \pm 1$, with $n \geq 0$ (e.g. Kukolich et al. 1973; Kukolich 1982; Boucher et al. 1977; Anttila et al. 1993; Šimečková et al. 2004; Cazzoli & Puzzarini 2006; Müller et al. 2009). Transitions with different K but the same J occur in narrow frequency regions but they have quite different energies (see Fig. 10).

We detected 18 lines of A-CH_3CN (in the $K = 0$ and 3 ladders) with $E_u/k \leq 184.4$ K, 23 lines for the E-CH_3CN (in the $K = 1$, 2, and 4 ladders) with $E_u/k \leq 199.0$ K, and three lines corresponding to several fully overlapped A-E transitions. Examples of line profiles of A- and E-CH_3CN lines are shown in

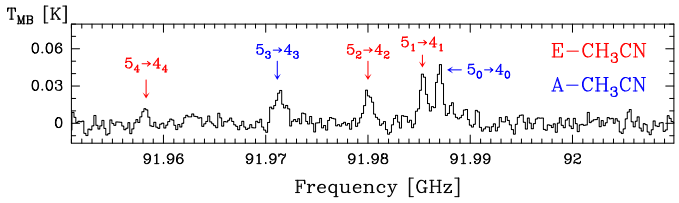

Fig. 10. Observed emission lines from the $J = 5 \rightarrow 4$ transitions of CH_3CN. Transitions with different K but the same J occur in narrow frequency regions despite they have different level energies.

Fig. 11. Table B.9 gives the observed line parameters. We did not detect the CH_3NC isomer (see Sect. 5.6).

3.9. Methanol: CH_3OH

Methanol, CH_3OH, is the simplest alcohol molecule. It is a slightly asymmetric rotor showing hindered internal rotation. Its energy levels are classified as a symmetric rotor with quantum number J_K and a threefold barrier that causes two states in the molecule, A and E; the latter being doubly degenerate (e.g. Lees & Baker 1968; Lees et al. 1973; Xu et al. 2008).

We detected 20 lines of A-CH_3OH (in the $|K| = 0$ and 1 ladders) with $E_u/k \leq 104.4$ K, 33 lines for the E-CH_3OH (in the $|K| = 1$, 2, 3, and 4 ladders) with $E_u/k \leq 114.8$ K, and two lines corresponding to several fully overlapped A-E transitions. Examples of line profiles of A- and E-CH_3OH lines are shown in Fig. 12. Table B.10 gives the observed line parameters.

3.10. Acetaldehyde: CH_3CHO

Acetaldehyde, CH_3CHO, is an asymmetric-top molecule with A and E symmetry states and a- and b-type transitions (e.g. Kleiner et al. 1996, and references therein).

We detected 18 lines of A-CH_3CHO, 15 lines of E-CH_3CHO, and three lines corresponding to a fully overlapped A-E transition (a-type transitions with $E_u/k \leq 109.7$ K). Figure 13 shows a selection of detected lines and Table B.11 gives the observed line parameters.

4. Spatial distribution of $C^{18}O$ and H_2CO

Figure 1 shows the spatial distribution of the rotationally excited $C^{18}O$ $J = 3 \rightarrow 2$ ($E_u/k \simeq 32$ K, $A_{ul} \simeq 2 \times 10^{-6}$ s^{-1}) and H_2CO $J_{K_a,K_c} = 5_{1,5} \rightarrow 4_{1,4}$ ($E_u/k \simeq 47$ K, $A_{ul} \simeq 1 \times 10^{-3}$ s^{-1}) lines along the Bar. The molecular dissociation front (DF) is traced by the vibrationally excited H_2 $v = 1 \rightarrow 0$ $S(1)$ line emission (H_2^*; black contours in Fig. 1; Walmsley et al. 2000). The red contours represent the O I fluorescent line at 1.32 μm (Walmsley et al. 2000) marking the position of the ionisation front (IF) that separates the H II region and the neutral cloud. The blue contours represent the $H^{13}CN$ $J = 1 \rightarrow 0$ emission tracing dense molecular clumps inside the Bar (Lis & Schilke 2003).

The emission from the Orion Bar can be distinguished from the extended OMC-1 cloud component by the emission LSR velocity. While OMC-1 is brighter in the 8−10 km s^{-1} velocity range, the Orion Bar emits predominantly in the 10−11 km s^{-1} range. The $C^{18}O$ and H_2CO line emissions shown in Fig. 1 are integrated in this latter interval. In these maps, H_2CO peaks at the position of the dense ($n(H_2) \simeq 6 \times 10^6$ cm^{-3}) and lukewarm ($T_k \simeq 50$ K) clumps inside the Bar (Lis & Schilke 2003). In addition, our maps reveal extended H_2CO emission along the PDR and close to the DF. This conclusion was initially inferred

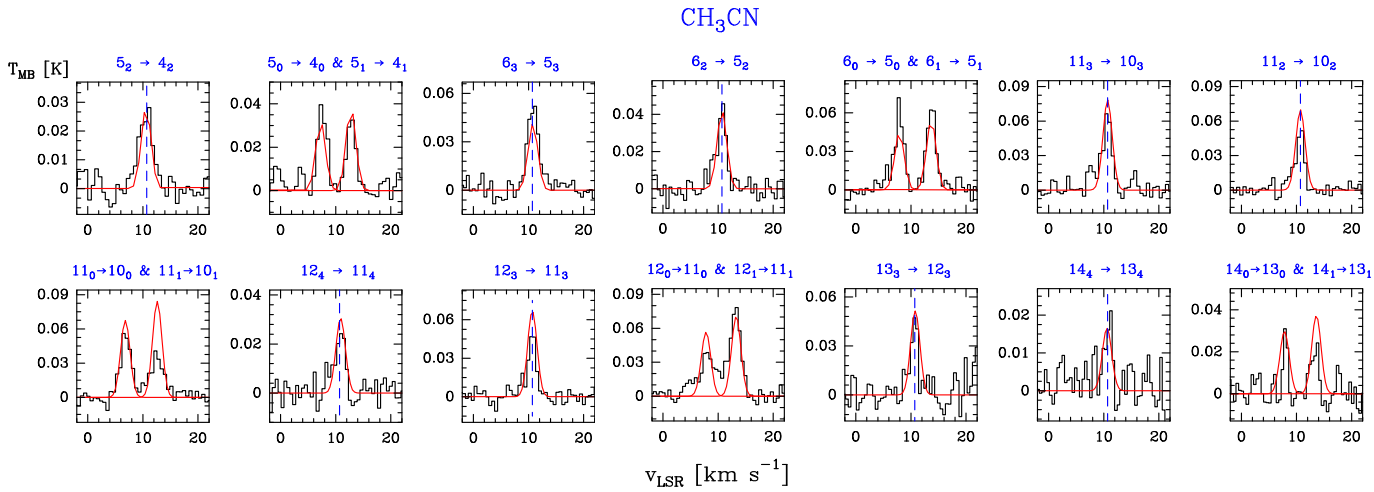

Fig. 11. Example of A- and E-CH_3CN lines (black histogram spectra). A non-LTE LVG model ($T_k \simeq 150$ K, $n(H_2) \simeq 1 \times 10^6$ cm^{-3}, N(A-CH_3CN) = 5×10^{11} cm^{-2}, and N(E-CH_3CN) = 6×10^{11} cm^{-2}) is shown overlaid in red (see Sect. 5.2).

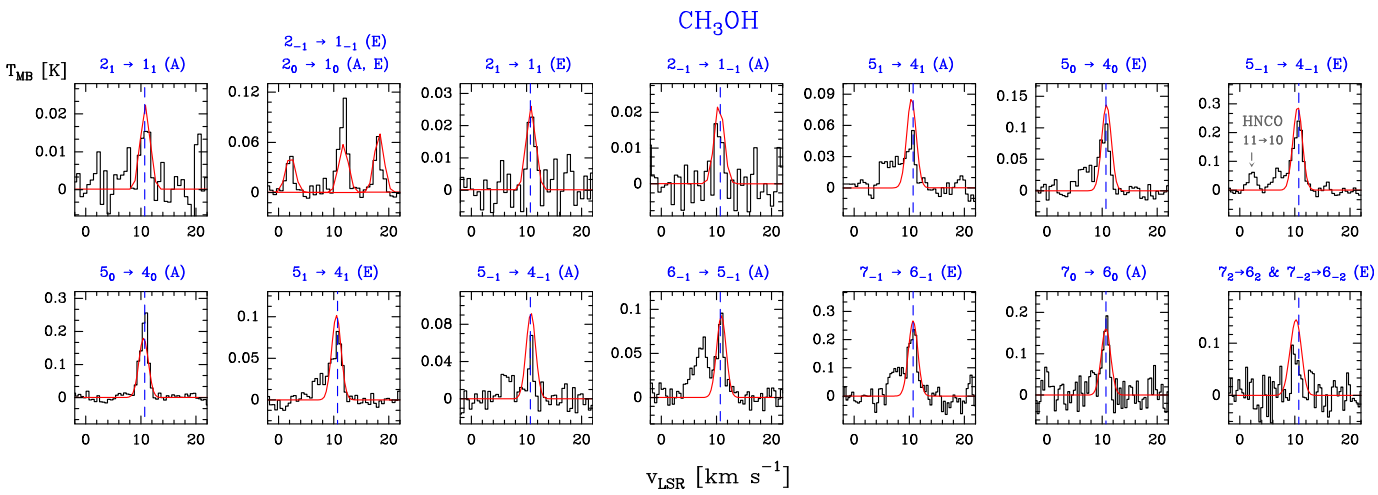

Fig. 12. Example of A- and E-CH_3OH lines (black histogram spectra). A non-LTE LVG model ($T_k \simeq 40$ K, $n(H_2) \simeq 3 \times 10^7$ cm^{-3}, N(A-CH_3OH) = 1.2×10^{13} cm^{-2}, and N(E-CH_3OH) = 1.9×10^{13} cm^{-2}) is shown overlaid in red (see Sect. 5.2).

by Leurini et al. (2010) from ~11″ resolution observations of lower-excitation H_2CO lines.

To investigate the chemical stratification as a function of FUV flux attenuation, we built averaged line intensity crosscuts perpendicular to the Bar. The maps were rotated by 50° to bring the incident FUV radiation from left, and then, line intensities in the mapped area were averaged parallel to the IF. In Fig. 14 we plot the resulting normalised intensity cuts as a function of distance to the IF position. Distances are in arcseconds and increase with depth into the molecular cloud. Although these cuts do not represent true abundance variations (different lines have different excitation conditions), to first order they can be used to study the chemical stratification in the PDR. The H_2^* emission peak is at ~15″ (vertical dot-dashed line) from the IF, and shows a narrow emission profile. The H_2CO $J_{K_a,K_c} = 5_{1,5} \rightarrow 4_{1,4}$ emission peak appears at ~27″, followed by $C^{18}O$ $J = 3 \rightarrow 2$ that peaks at ~35″.

We note that the different position of the emission peaks of the $C^{18}O$ $J = 3 \rightarrow 2$ and H_2CO $J_{K_a,K_c} = 5_{1,5} \rightarrow 4_{1,4}$ lines shown in Fig. 14 could be related to a sharp thermal gradient in the region, with the gas temperature increasing from ~50 K inside the dense clumps seen in the PDR interior (Lis & Schilke 2003), to ~300 K near the DF. The H_2CO $J_{K_a,K_c} = 5_{1,5} \rightarrow 4_{1,4}$ line requires higher excitation conditions (higher temperature/density) and thus it would naturally peak closer to the DF than the $C^{18}O$ $J = 3 \rightarrow 2$ line, even for constant H_2CO and $C^{18}O$ abundances throughout the PDR. Still, the main point is that observations show that H_2CO is present in the warm interclump gas and close to the PDR edge where the FUV flux is strong.

5. Analysis

5.1. Line parameter fitting procedure

Detected lines show simple Gaussian line profiles centred at the Orion Bar LSR velocity and thus Gaussian profiles were fitted to all detected lines. For the resolved and unblended COM lines detected with significant S/N, the mean line width is $\Delta v = 1.8$ km s^{-1}, with a standard deviation of $\sigma = 0.6$ km s^{-1}.

The spectroscopic and observational line parameters of the detected lines are given in Tables B.1–B.11. We provide line frequencies (in MHz), energy of the upper level of each transition (E_u/k in K), Einstein coefficient for spontaneous emission (A_{ul} in s^{-1}), intrinsic line strength (S_{ul}), and the level degeneracy (g_u) from the MADEX spectral catalogue, and the JPL and CDMS molecular databases. The velocity-integrated intensity ($\int T_{MB} dv$ in mK km s^{-1}), LSR velocity (v_{LSR} in km s^{-1}), FWHM

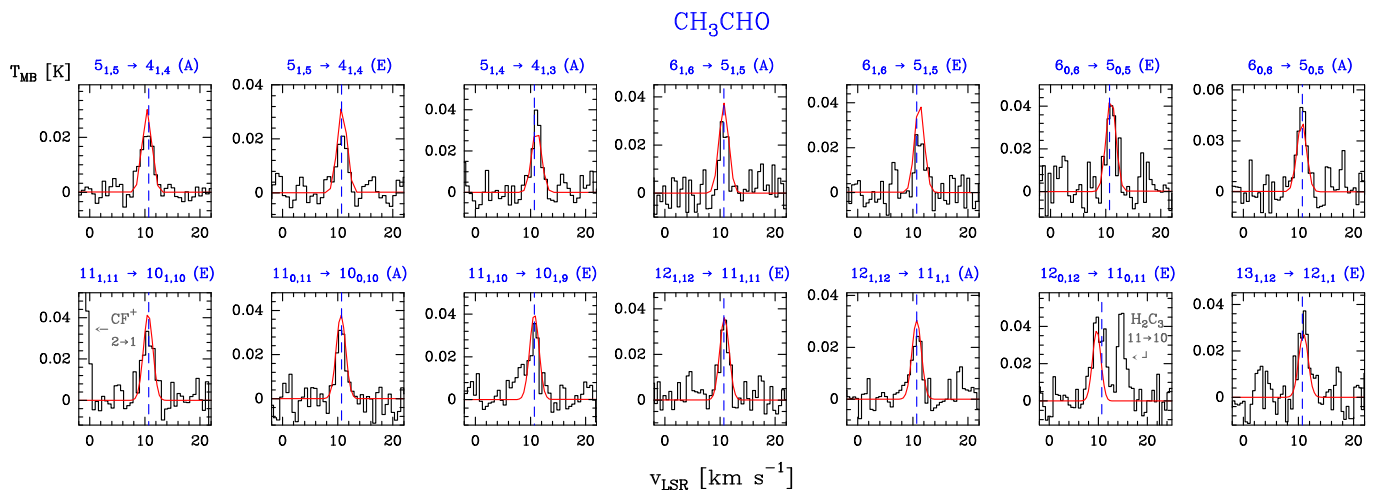

Fig. 13. Examples of A- and E-CH_3CHO lines (black histogram spectra). Single excitation temperature models are shown overlaid in red (see Sect. 5.4).

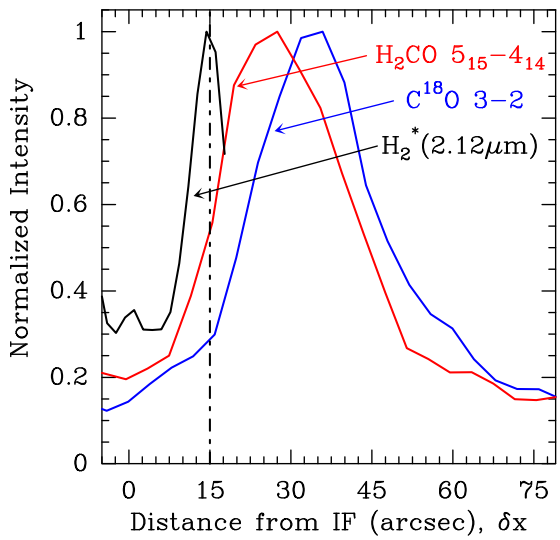

Fig. 14. Normalised intensity crosscuts for $C^{18}O$ $J = 3 \rightarrow 2$ (blue curve), H_2CO $J_{K_a,K_c} = 5_{1,5} \rightarrow 4_{1,4}$ (red curve), and H_2^* (black curve) as a function of distance from the IF (in arcsec). The vertical dot-dashed line indicates the H_2 dissociation front. FUV radiation comes from left.

Table 3. Best fit LVG model parameters and comparison with the column density obtained with the rotational diagram (RD) analysis.

	LVG calculations			RD analysis*
	T_k [K]	$n(H_2)$ [cm^{-3}]	$N(X)_{LVG}$ [cm^{-2}]	$N(X)_{RD}$ [cm^{-2}]
o-H_2CO	~200	~10^6	4.0×10^{13}	$(4.4 \pm 0.6) \times 10^{13}$
p-H_2CO	~200	~10^6	1.8×10^{13}	$(1.6 \pm 0.1) \times 10^{13}$
HC_3N	~80	~10^6	4.0×10^{11}	$(4.2 \pm 0.3) \times 10^{11}$
A-CH_3CN	~150	~10^6	5.0×10^{11}	$(5.8 \pm 0.8) \times 10^{11}$
E-CH_3CN	~150	~10^6	6.0×10^{11}	$(5.7 \pm 0.7) \times 10^{11}$
E-CH_3OH	~40	~3×10^7	1.9×10^{13}	$(1.9 \pm 0.2) \times 10^{13}$

Notes. (*) Rotational diagram analysis assuming uniform beam filling (see Sect. 5.4).

(full width at half maximum) line width (Δv in km s^{-1}), and the line peak temperature (T_{MB} in mK) were obtained from Gaussian fits. Parentheses indicate the uncertainty. When two or more transitions were found to be overlapping, the total profile was fitted. Fully overlapping transitions are marked with connecting symbols in the tables.

5.2. Non-LTE LVG excitation analysis: physical conditions

We estimate the beam-averaged physical conditions towards the line survey position from non-LTE (local thermodynamic equilibrium) excitation models for molecules with known inelastic collisional rate coefficients (H_2CO, HC_3N, CH_3CN, and CH_3OH)[4]. In particular, we run a large grid of non-LTE excitation and radiative transfer models in which the statistical equilibrium equations are explicitly solved in the LVG (large velocity gradient) approximation using MADEX (Cernicharo 2012; see also Appendix A in Cuadrado et al. 2015).

We tested a broad range of column density (N), H_2 density ($n(H_2)$ = 10^3–10^9 cm^{-3}), and gas temperature (T_k = 10−1000 K) values. We adopted Δv = 2 km s^{-1} line widths. In order to constrain the physical conditions that reproduce the observed line intensities and line profiles towards the observed position, we compared the observed H_2CO, CH_3OH, CH_3CN, and HC_3N lines to synthetic lines obtained from the grid of LVG models. The best fit model (assuming uniform beam filling emission) was obtained by finding the minimum root mean square (rms); we refer to Cuadrado et al. (2015) for a detailed explanation. The range of column densities that we used as an input in the models is around the value derived from the rotational diagrams analysis (see Sect. 5.4). In fact, the best fit models have column densities within a factor of 2 (see Table 3) of the inferred value from the rotational diagram analysis (we note that in these models the observed lines are optically thin). Figure 15 represents the rms_{min}/rms ratio as a function of T_k and $n(H_2)$ for a grid of excitation models trying to fit the observed lines towards the PDR position.

[4] We used [H_2CO–H_2] collisional rates for ortho and para H_2CO (Green 1991), [A/E-CH_3OH–H_2] for A- and E-CH_3OH (Rabli & Flower 2010), [A/E-CH_3CN–H_2] for A- and E-CH_3CN (Green 1986), and [HC_3N–H_2] for HC_3N (Wernli et al. 2007).

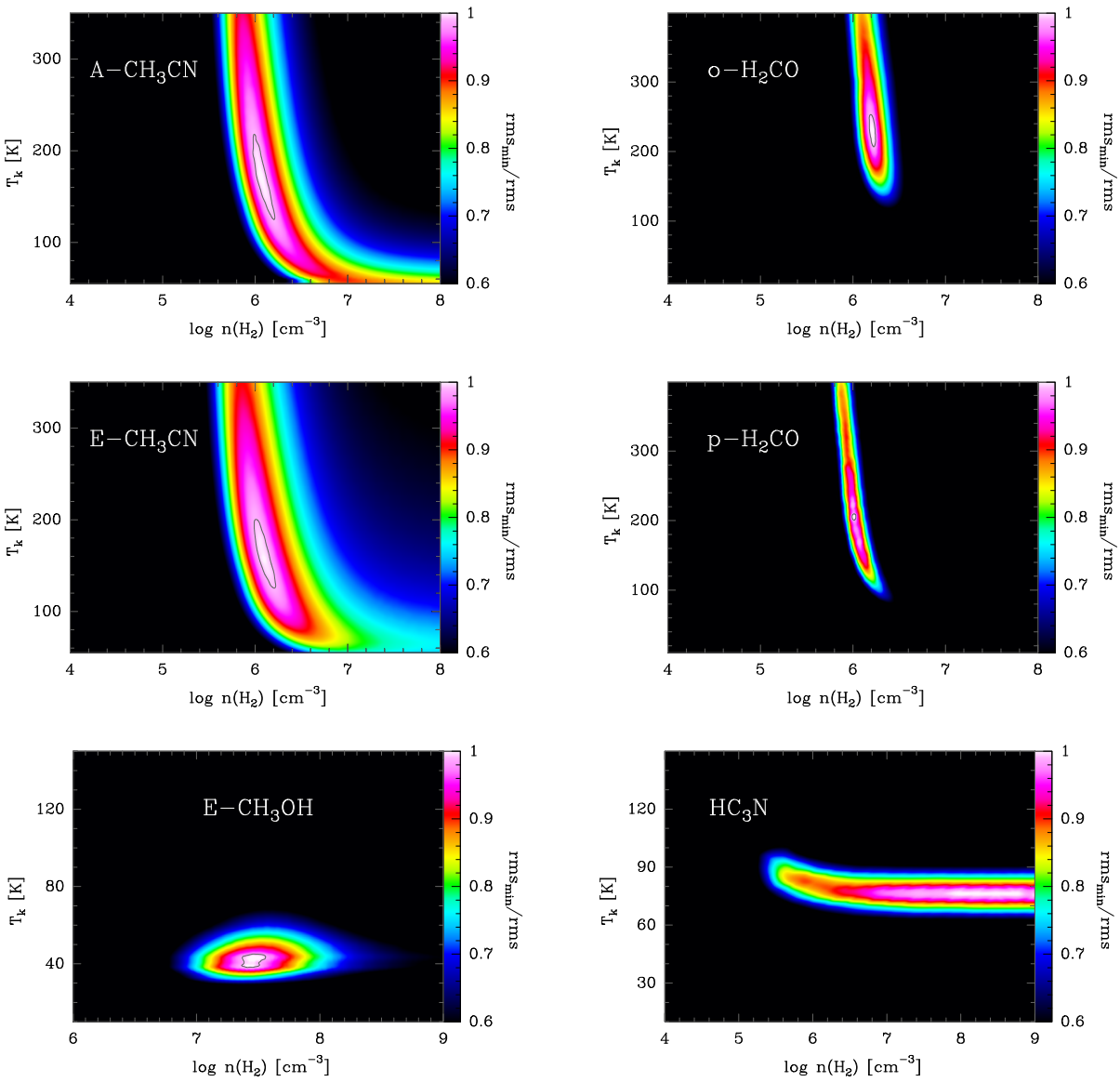

Fig. 15. Grid of LVG excitation and radiative transfer models for CH_3CN, H_2CO, CH_3OH, and HC_3N lines towards the PDR position assuming uniform beam filling and using column densities shown in Table 3. The best fits are those with the higher rms_{min}/rms value.

From the excitation analysis it seems that not all COMs arise from the same PDR layers (i.e. same cloud depth). The set of beam-averaged physical conditions that best fit the CH_3CN and H_2CO lines lie within $T_k = 150–250$ K and $n(H_2) = (1–3) \times 10^6$ cm^{-3}, similar (although slightly denser gas) to that obtained for C_2H in Cuadrado et al. (2015). Figures 3 and 11 show the best fit models overlaid over the observed lines. The HC_3N detected lines (see Fig. 9) fit within $T_k = 70–90$ K and $n(H_2) > 1 \times 10^6$ cm^{-3}. The physical conditions that fit the CH_3OH detected lines (see Fig. 12) are colder and denser ($T_k = 40–50$ K and $n(H_2) \simeq 5 \times 10^7$ cm^{-3}). The best-fit parameters ($n(H_2)$, T_k, and N) of the LVG models fitting the lines in Figs. 3, 9, 11, and 12 are shown in Table 3. We note, however, that the best fit gas density value depends on the assumed emission beam filling factor[5] for each molecule. Lower densities (by a factor of up to ~10) would still be consistent with observations if one assumes a semi-extended emission source (i.e. more compact than the beam-size at each observed frequency; see Sect. 5.4).

Higher-angular-resolution maps are needed to spatially resolve the structures producing the molecular emission (Goicoechea et al. 2016). Either way, CH_3OH and HC_3N seem to arise from a different, cooler component where the FUV flux has been attenuated. This scenario agrees with the different H_2CO and CH_3OH spatial distributions observed by Leurini et al. (2010) with the IRAM 30 m telescope and the PdB interferometer. In particular, Leurini et al. found that both species show different spatial distributions, with CH_3OH only tracing the denser and cooler clumps seen deeper inside the Bar, whereas H_2CO also traces the warmer extended (interclump) gas directly exposed to the strong FUV-field. Consistent with previous works (Goicoechea et al. 2011, 2016; Nagy et al. 2013),

[5] Assuming that the emission source has a 2D Gaussian shape, the beam filling factor (η_{bf}) is equal to $\eta_{bf} = \theta_S^2/(\theta_S^2 + \theta_B^2)$, with θ_B the HPBW of the 30 m telescope (in arcsec) and θ_S the diameter of the Gaussian source (also in arcsec). For the semi-extended emission we assumed that $\theta_S = 9''$ (see Sect. 5.4).

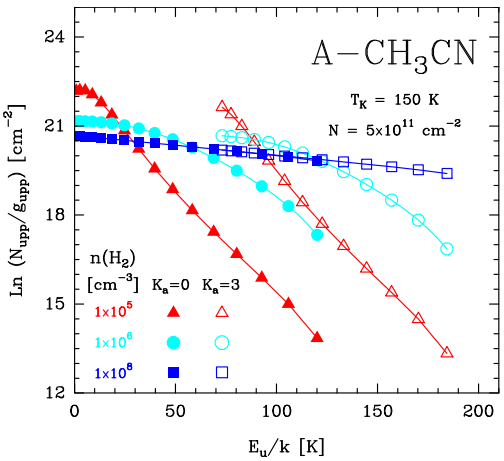

Fig. 16. Rotational population diagrams for A-CH_3CN computed with a non-LTE excitation code. All models adopt the same gas temperature (T_k = 150 K) and column density ($N_{tot} = 5 \times 10^{11}$ cm^{-2}), but three different $n(H_2)$ values. For simplicity, only rotational transitions in the $K_a = 0$ (filled symbols) and 3 (empty symbols) ladders are shown.

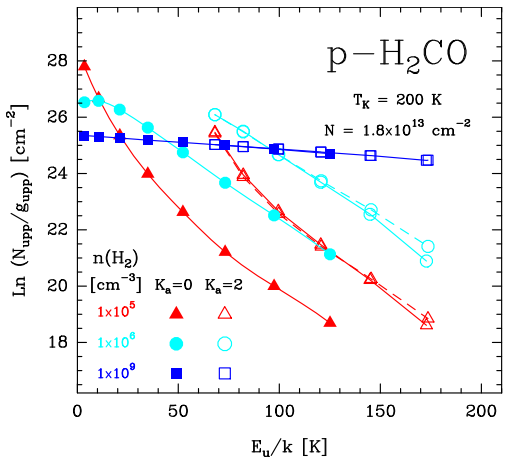

Fig. 17. Rotational population diagrams for p-H_2CO computed with a non-LTE excitation code. All models adopt the same gas temperature (T_k = 200 K) and column density ($N_{tot} = 1.8 \times 10^{13}$ cm^{-2}), but three different $n(H_2)$ values. For simplicity, only rotational transitions in the $K_a = 0$ (filled symbols) and 2 (empty symbols) ladders are shown. We note that at densities <10^8 cm^{-3}, the set of transitions with the $K_a = 2$ number are also split into two components: (i) transitions with $K_c = J$–1 (empty symbols connected with solid lines) and (ii) transitions with $K_c = J$–2 (empty symbols connected with dashed lines).

we derive very high thermal gas pressures at the PDR edge ($P_{th}/k = n_H T_K \gtrsim 10^8$ K cm^{-3}).

5.3. Subthermal excitation effects on the rotational diagrams of symmetric- and asymmetric-top molecules

In this section we show how subthermal excitation effects modify the resulting rotational population diagram of symmetric- and asymmetric-top molecules such as CH_3CN and H_2CO, respectively. In particular we run a grid of LVG models for varying gas densities, but keeping the same gas temperature and column density. Figures 16 and 17 show model results in the form of population diagrams for A-CH_3CN transitions in the $K_a = 0$ and 3 rotational ladders (T_k = 150 K and $N_{tot} = 5 \times 10^{11}$ cm^{-2}), and for p-H_2CO in the $K_a = 0$ and 2 rotational ladders (T_k = 200 K and $N_{tot} = 1.8 \times 10^{13}$ cm^{-2}). Only at very high gas densities, higher than the critical density for collisional excitation ($n \gg n_{cr}$), do inelastic collisions drive the level populations close to LTE ($T_{rot} \simeq T_k$). In a rotational diagram, the K_a ladders merge in a single straight line with a slope equal to $-1/T_k$. Owing to the high gas densities, this characteristic straight diagram is typically seen towards hot cores (e.g. Bisschop et al. 2007). As the gas density decreases, the excitation becomes subthermal ($T_{rot} < T_k$), and the rotational population diagram starts to show separate rotational ladders for each set of transitions with the same K_a quantum number. For very polar molecules such as CH_3CN and H_2CO (thus high n_{cr}), subthermal excitation happens at relatively high densities. Therefore, accurate column densities and rotational temperatures from rotational diagrams can only be obtained if the individual column densities for each rotational ladder are computed independently. This likely explains the discrepancy with the high T_{rot} obtained by Nagy et al. (2017) in the rotational diagram of their submm o-H_2CO lines observed with *Herschel*/HIFI towards the Bar.

5.4. Rotational diagrams and column-density determination

We determined the beam-averaged column density (N) and the rotational temperature (T_{rot}) for each molecule found by building rotational diagrams (e.g. Goldsmith & Langer 1999; Cuadrado et al. 2015). The large number of detected lines allows us to accurately determine rotational temperatures and column densities. Optically thin emission is assumed (consistent with our best LVG models of H_2CO, HC_3N, CH_3CN, and CH_3OH). We note that owing to their specific spectroscopy and prevailing excitation conditions at the edge of the Bar (subthermal excitation), a correct determination of the rotational temperatures and column densities for species such as H_2CO, H_2CS, H_2CCO, CH_3OH, and CH_3CN requires building specific diagrams for each rotational ladder (see Sect. 5.3). For the molecules with known collisional rates, we determine $N_{LVG} \approx N_{RD}$ (within a factor of 2). This comparison shows that the N_{RD} computed for the other molecules are accurate.

The rotational diagrams were built considering two limiting cases: (i) that the detected emission is extended (i.e. uniform beam filling), with $\eta_{bf} = 1$; and (ii) that the emission is semi-extended, assuming that $\theta_s = 9''$ (the typical beam of the IRAM 30 m telescope at ~1 mm)[6]. We only considered lines not blended with other transitions and detected above a 3σ level. The resulting rotational diagrams are shown in Fig. 18. Rotational temperatures and column densities obtained by linear least squares fits are listed in Table 4. The uncertainties shown in Table 4 indicate the uncertainty obtained from the least squares fit to the rotational diagram. The uncertainty obtained in the determination of the line parameters with the Gaussian fitting programme are included in the uncertainty bars at each point of the rotational diagram.

For H_2CO, $H_2^{13}CO$, H_2CS, H_2CCO, A-CH_3OH, A-CH_3CN, and E-CH_3CN we have built specific rotational diagrams for different sets of transitions with the same K_a quantum number value. The total column density of the molecule is obtained by adding the column density of each rotational ladder. For the other molecules, it is possible to fit the observed transitions by a single T_{rot} and N, independently of the K_a value. The cis- and trans-HCOOH rotational diagrams are shown in Cuadrado et al. (2016).

For molecules with hyperfine structure, like that of HCO, each rotational transition was described without splits, only with a single rotational number N. For this purpose, the integrated intensity, W, level degeneracy, g, and line strength, S, of each transition was calculated as the sum of all allowed hyperfine

Table 4. Rotational temperatures (T_{rot}), column densities (N), and abundances with respect to hydrogen nuclei inferred in the Orion Bar PDR.

	Uniform beam filling		Semi-extended source			
	T_{rot} [K]	N(X) [cm^{-2}]	T_{rot} [K]	N(X) [cm^{-2}]	Abundance*	Notes
HCO	15 ± 2	$(1.1 \pm 0.3) \times 10^{13}$	9 ± 2	$(5.3 \pm 3.5) \times 10^{13}$	$(1.7–8.4) \times 10^{-10}$	a
o-H_2CO $K_a = 1$	17 ± 2	$(3.7 \pm 0.6) \times 10^{13}$	12 ± 1	$(1.1 \pm 0.3) \times 10^{14}$		a
o-H_2CO $K_a = 3$	17	$(6.9 \pm 1.0) \times 10^{12}$	12	$(1.1 \pm 0.2) \times 10^{13}$		b, c
p-H_2CO $K_a = 0$	16 ± 2	$(9.8 \pm 1.4) \times 10^{12}$	9 ± 1	$(3.9 \pm 0.6) \times 10^{13}$		a, c
p-H_2CO $K_a = 2$	18 ± 1	$(6.2 \pm 0.2) \times 10^{12}$	13 ± 1	$(1.3 \pm 0.1) \times 10^{13}$		a, c
[(o+p)-H_2CO]	–	$(6.0 \pm 0.6) \times 10^{13}$	–	$(1.7 \pm 0.3) \times 10^{14}$	$(0.9–2.7) \times 10^{-9}$	d
o-$H_2^{13}CO$	15 ± 3	$(7.3 \pm 2.4) \times 10^{11}$	10 ± 2	$(3.0 \pm 1.1) \times 10^{12}$		a
p-$H_2^{13}CO$	9 ± 1	$(2.3 \pm 0.4) \times 10^{11}$	7 ± 1	$(8.0 \pm 1.2) \times 10^{11}$		a, c
[(o+p)-$H_2^{13}CO$]	–	$(9.6 \pm 2.4) \times 10^{11}$	–	$(3.8 \pm 1.1) \times 10^{12}$	$(1.5–6.0) \times 10^{-11}$	d
o-H_2CS $K_a = 1$	30 ± 3	$(3.1 \pm 0.5) \times 10^{12}$	19 ± 1	$(1.3 \pm 0.2) \times 10^{13}$		a
o-H_2CS $K_a = 3$	30	$(6.7 \pm 1.9) \times 10^{11}$	19	$(2.7 \pm 0.4) \times 10^{12}$		e, c
p-H_2CS $K_a = 0$	29 ± 6	$(5.0 \pm 1.4) \times 10^{11}$	16 ± 2	$(2.6 \pm 1.0) \times 10^{12}$		a
p-H_2CS $K_a = 2$	35 ± 8	$(7.8 \pm 4.4) \times 10^{11}$	15 ± 3	$(2.6 \pm 1.9) \times 10^{12}$		a
[(o+p)-H_2CS]	–	$(5.0 \pm 0.7) \times 10^{12}$	–	$(2.1 \pm 0.3) \times 10^{13}$	$(0.8–3.3) \times 10^{-10}$	d
HNCO	51 ± 7	$(1.0 \pm 0.1) \times 10^{12}$	26 ± 3	$(5.6 \pm 1.3) \times 10^{12}$	$(1.6–8.9) \times 10^{-11}$	a
CH_2NH	28 ± 7	$(1.1 \pm 0.4) \times 10^{12}$	27 ± 7	$(2.4 \pm 1.0) \times 10^{12}$	$(1.7–3.8) \times 10^{-11}$	a
o-H_2CCO $K_a = 1$	55 ± 2	$(3.0 \pm 0.1) \times 10^{12}$	30 ± 2	$(1.3 \pm 0.2) \times 10^{13}$		a
o-H_2CCO $K_a = 3$	64 ± 6	$(1.3 \pm 0.3) \times 10^{12}$	34 ± 1	$(4.2 \pm 0.7) \times 10^{12}$		a
p-H_2CCO $K_a = 0$	57 ± 4	$(4.8 \pm 0.6) \times 10^{11}$	42 ± 3	$(1.3 \pm 0.2) \times 10^{12}$		a
p-H_2CCO $K_a = 2$	54 ± 3	$(1.1 \pm 0.1) \times 10^{12}$	29 ± 2	$(6.1 \pm 1.8) \times 10^{12}$		a
[(o+p)-H_2CCO]	–	$(5.9 \pm 0.3) \times 10^{12}$	–	$(2.5 \pm 0.3) \times 10^{13}$	$(0.9–4.0) \times 10^{-10}$	d
HC_3N	43 ± 2	$(4.2 \pm 0.3) \times 10^{11}$	27 ± 1	$(3.2 \pm 0.3) \times 10^{12}$	$(0.7–5.1) \times 10^{-11}$	a
cis-HCOOH	23 ± 4	$(4.6 \pm 0.7) \times 10^{11}$	21 ± 4	$(4.2 \pm 0.6) \times 10^{12}$		f
trans-HCOOH $K_a = 0$	12 ± 2	$(3.5 \pm 0.5) \times 10^{11}$	6 ± 1	$(4.1 \pm 0.6) \times 10^{12}$		f
trans-HCOOH $K_a = 1$	12 ± 3	$(3.3 \pm 1.3) \times 10^{11}$	6 ± 1	$(3.6 \pm 2.1) \times 10^{12}$		f
trans-HCOOH $K_a = 2$	13 ± 3	$(6.3 \pm 2.8) \times 10^{11}$	7 ± 1	$(5.0 \pm 2.4) \times 10^{12}$		f
[(cis+trans)-HCOOH]	–	$(1.8 \pm 0.3) \times 10^{12}$	–	$(1.7 \pm 0.3) \times 10^{13}$	$(0.3–2.7) \times 10^{-10}$	g
A-CH_3CN $K_a = 0$	26 ± 2	$(2.8 \pm 0.5) \times 10^{11}$	19 ± 1	$(1.9 \pm 0.6) \times 10^{12}$		a
A-CH_3CN $K_a = 3$	30 ± 1	$(3.0 \pm 0.6) \times 10^{11}$	21 ± 1	$(1.5 \pm 0.6) \times 10^{12}$		a
E-CH_3CN $K_a = 1$	28 ± 2	$(2.9 \pm 0.5) \times 10^{11}$	20 ± 1	$(1.8 \pm 0.4) \times 10^{12}$		a
E-CH_3CN $K_a = 2$	31 ± 1	$(1.7 \pm 0.2) \times 10^{11}$	22 ± 1	$(1.0 \pm 0.3) \times 10^{12}$		a
E-CH_3CN $K_a = 4$	26 ± 1	$(1.1 \pm 0.4) \times 10^{11}$	18 ± 1	$(6.7 \pm 3.2) \times 10^{11}$		a
[(A+E)-CH_3CN]	–	$(1.2 \pm 0.1) \times 10^{12}$	–	$(6.9 \pm 1.0) \times 10^{12}$	$(0.2–1.1) \times 10^{-10}$	h
A-CH_3OH $K_a = 0$	34 ± 2	$(8.0 \pm 0.6) \times 10^{12}$	18 ± 2	$(5.3 \pm 1.1) \times 10^{13}$		a
A-CH_3OH $K_a = \pm 1$	26 ± 2	$(3.5 \pm 0.9) \times 10^{12}$	14 ± 1	$(2.8 \pm 0.7) \times 10^{13}$		a
E-CH_3OH	36 ± 3	$(1.9 \pm 0.2) \times 10^{13}$	26 ± 3	$(6.5 \pm 1.4) \times 10^{13}$		a
[(A+E)-CH_3OH]	–	$(3.1 \pm 0.2) \times 10^{13}$	–	$(1.5 \pm 0.2) \times 10^{14}$	$(0.5–2.4) \times 10^{-9}$	h
A-CH_3CHO	31 ± 2	$(2.3 \pm 0.3) \times 10^{12}$	20 ± 1	$(1.2 \pm 0.2) \times 10^{13}$		a
E-CH_3CHO	33 ± 3	$(2.6 \pm 0.4) \times 10^{12}$	21 ± 1	$(1.2 \pm 0.2) \times 10^{13}$		a
[(A+E)-CH_3CHO]	–	$(4.9 \pm 0.5) \times 10^{12}$	–	$(2.4 \pm 0.3) \times 10^{13}$	$(0.8–3.8) \times 10^{-10}$	h

Notes. (*) The abundance of each species with respect to H nuclei is given by $\frac{N(X)}{N_H} = \frac{N(X)}{N(H)+2N(H_2)}$, with $N(H_2) \simeq 3 \times 10^{22}$ cm^{-2} and $N(H) \simeq 3 \times 10^{21}$ cm^{-2} (van der Werf et al. 2013). (a) T_{rot} and N from rotational diagram analysis. (b) Only two lines detected with the same E_u/k. N calculated assuming the same T_{rot} that o-H_2CO $K_a = 1$. (c) ΔN estimated assuming a 15% of the calculated N. (d) Total N calculated as the sum of the ortho and para species. (e) Only two lines detected with upper level energies of 138.3 K and 149.8 K. They are too similar for an accurate estimation of T_{rot} and N from a rotational diagram analysis. N calculated assuming the same T_{rot} that o-H_2CS $K_a = 1$. (f) From Cuadrado et al. (2016). (g) Total N calculated as the sum of the cis and trans species. (h) Total N calculated as the sum of the A and E species.

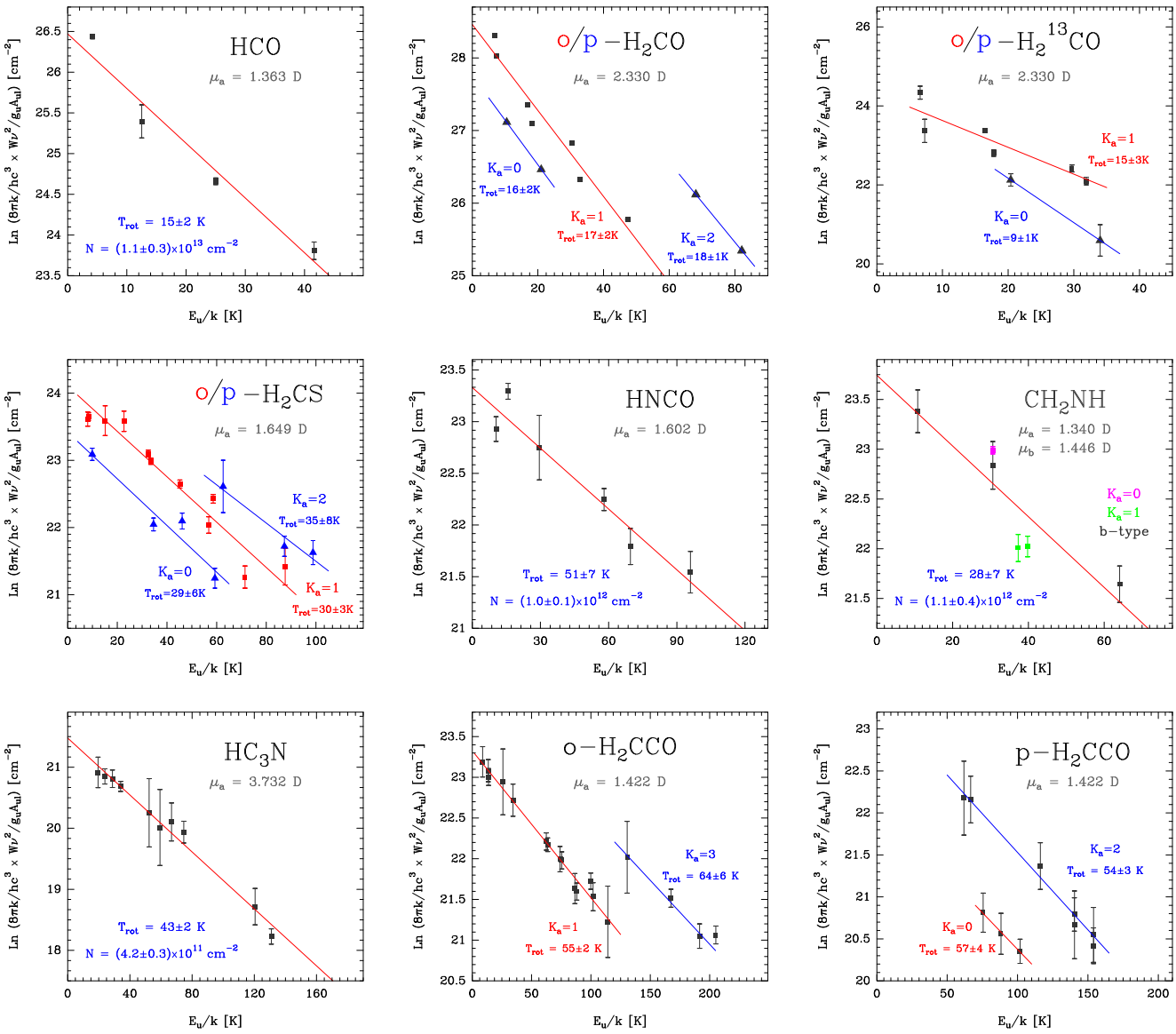

Fig. 18. Rotational diagrams of the detected complex molecules in the Orion Bar PDR (assuming uniform beam filling). Fitted values of the rotational temperature, $T_{\rm rot}$, column density, N, and their respective uncertainties are also indicated for each molecule.

components of each $N{+}1 \rightarrow N$ transition. The characteristic frequency, ν, was determined using the weighted average with the relative strength of each line as weight, and the Einstein coefficient, A, was calculated using the weighted values in the usual relation.

Comparing the resulting rotational diagrams, we see that: (i) H_2CO and CH_3OH are, by far, the most abundant organic molecules (by a factor of $\gtrsim$5), followed by HCO, H_2CCO, CH_3CHO, H_2CS, HCOOH, CH_3CN, CH_2NH, HNCO, $H_2^{13}CO$, and HC_3N (in decreasing order of abundance); (ii) the ortho-to-para (OTP) ratios obtained from the H_2CO, $H_2^{13}CO$, H_2CS, H_2CCO column densities are ~3, as expected at high gas temperature; (iii) we obtain similar rotational temperatures for ortho-para and A-E species; (iv) and the inferred $[H_2CO]/[H_2^{13}CO]$ ratio is 63 ± 3, similar to the $^{12}C/^{13}C \approx 67$ isotopic ratio in Orion (Langer & Penzias 1990). Hence, this confirms that even lines from the most abundant organic species studied in this work, are optically thin.

In order to confirm the correct line identification and possible line blendings, we have modelled the spectrum of each molecule using the MADEX radiative transfer code assuming a Boltzmann distribution and a single excitation temperature for the rotational levels population (we recall that for the observed set of lines/ladders of a given molecule, we infer a single temperature component from the rotational diagrams). Figures 2, and 5–8, and 13 show the observational spectra (black histograms) and the modelled spectra (red lines) of each molecule. The obtained fits agree very well with the observations and rotational diagrams.

5.5. Abundances

In order to determine molecular abundances with respect to hydrogen nuclei[6] towards the line survey position, we derived the beam-averaged H_2 column density from our observations of the optically thin $C^{18}O$ lines ($J = 1 \rightarrow 0$, $2 \rightarrow 1$, and $3 \rightarrow 2$ transitions) assuming $^{16}O/^{18}O \approx 500$ (Wilson & Rood 1994) and

[6] The molecular abundance with respect to hydrogen nuclei is given by $\frac{N(X)}{N(H)+2N(H_2)}$.

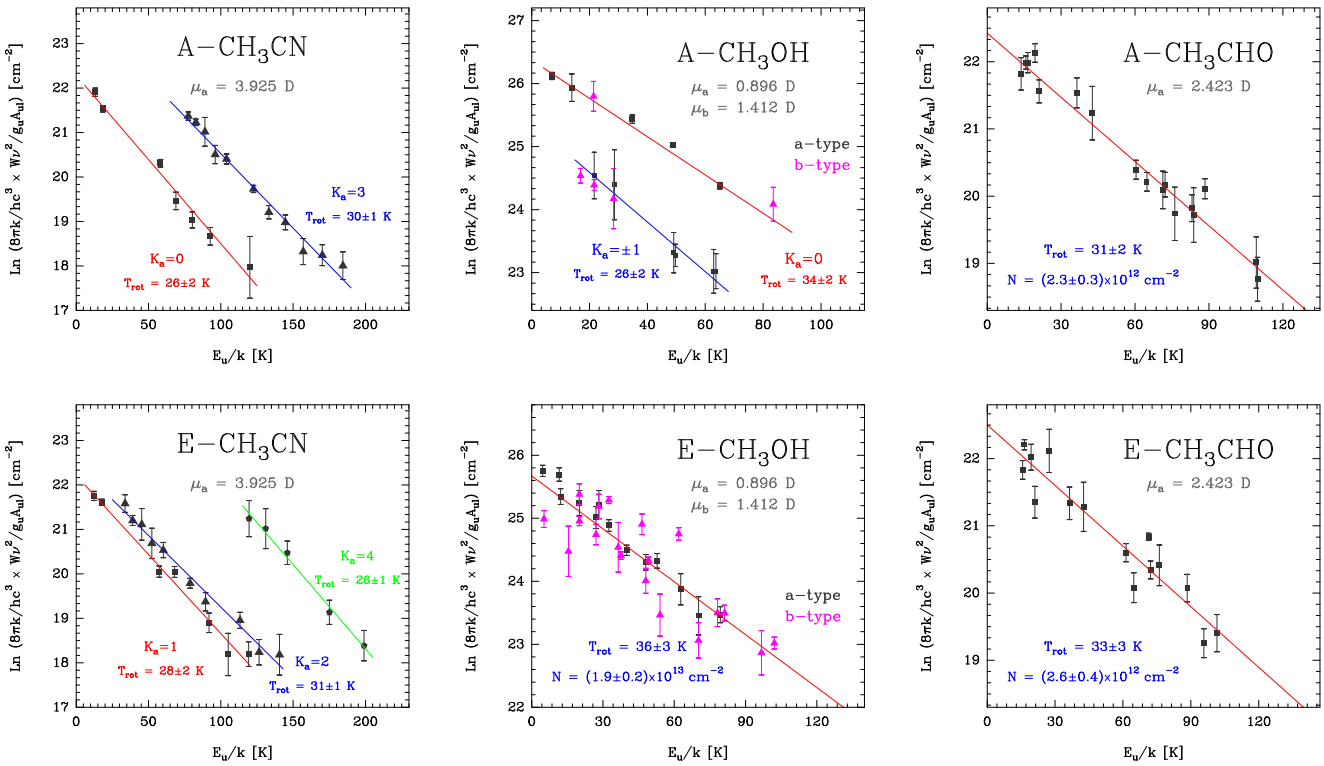

Fig. 18. continued.

a [CO]/[H_2] abundance of $\sim 10^{-4}$ (lower than the canonical value due to photodissociation). The resulting H_2 column density, $N(H_2) \simeq 3 \times 10^{22}$ cm^{-2}, is in good agreement with previous estimations of $N(H_2)$ close to the dissociation front (see e.g. Hogerheijde et al. 1995). A hydrogen atom column density, N(H), of $\sim 3 \times 10^{21}$ cm^{-2} has been inferred from H I observations towards the edge of the Orion Bar (van der Werf et al. 2013). Molecular abundances with respect to hydrogen nuclei are listed in Table 4. The abundances of the detected species range from 10^{-9} to 10^{-11}.

5.6. Undetected complex organic molecules and precursors

The broadband frequency coverage of the survey allowed us to obtain upper limits for other chemically interesting organic molecules that have not been detected towards the edge of the PDR, but could have been expected. In particular, we searched for HDCO, CH_3O, CH_3NC, CH_3CCH, CH_3OCH_3, $HCOOCH_3$, CH_3CH_2OH, CH_2CHCN, and CH_3CH_2CN, because they have been detected in other PDRs and star-forming regions (e.g. Horsehead, Orion KL, Barnard 1-b, or IRAS 16293-2422; see Table 6 for references). The CH_3O radical is thought to be an important intermediary for the H_2CO and CH_3OH chemistry but so far, has only been detected in cold and dense gas (Cernicharo et al. 2012; Bacmann & Faure 2016). HDCO has been detected by Parise et al. (2009) towards the lukewarm, dense and more FUV-shielded clump #3 of Lis & Schilke (2003), but it is not detected towards the warmer and high FUV-illuminated line survey position, near the dissociation front.

First, we estimated 3σ line intensities using the relation

$$\int T_{\rm MB}\,{\rm d}v = 3\sigma\sqrt{2\,\delta v\,\Delta v} \qquad [{\rm K\,km\,s^{-1}}], \tag{1}$$

Table 5. Upper limits for undetected COMs.

Molecule	N(X) [cm^{-2}]	Abundance^a
HDCO^b	$(1.3–1.5) \times 10^{11}$	$(2.1–2.4) \times 10^{-12}$
CH_3O	$(2.0–4.0) \times 10^{12}$	$(3.2–6.3) \times 10^{-11}$
CH_3NC	$(5.0–8.0) \times 10^{10}$	$(0.8–1.3) \times 10^{-12}$
CH_3CCH	$(5.0–8.0) \times 10^{12}$	$(0.8–1.3) \times 10^{-10}$
CH_3OCH_3	$(7.0–9.0) \times 10^{12}$	$(1.1–1.4) \times 10^{-10}$
$HCOOCH_3$	$(9.0–9.5) \times 10^{12}$	$(1.4–1.5) \times 10^{-10}$
CH_3CH_2OH	$(1.0–1.2) \times 10^{12}$	$(1.6–1.9) \times 10^{-11}$
CH_2CHCN	$(9.0–9.5) \times 10^{12}$	$(1.4–1.5) \times 10^{-10}$
CH_3CH_2CN	$(7.0–5.0) \times 10^{11}$	$(1.1–0.8) \times 10^{-11}$

Notes. [a] The abundance of each species with respect to H nuclei (see Sect. 5.5). [b] Detected by Parise et al. (2009) towards clump #3 (Lis & Schilke 2003) of the Orion Bar.

where σ is the rms of the observations per resolution channel [K], δv is the velocity spectral resolution [km s^{-1}], and Δv is the assumed line widths ($\sim$2 km s^{-1}). Second, we used MADEX to create synthetic models that simulate the line emission to constrain their column densities. The column densities and 3σ upper limit abundances assuming $T_{\rm rot} = 20–30$ K are listed in Table 5. We also provide the following abundance ratio upper limits: [HDCO]/[H_2CO] < 0.003 and [CH_3NC]/[CH_3CN] < 0.1. Parise et al. (2009) estimated an abundance ratio of [HDCO]/[H_2CO] > 0.006 towards clump #3, which suggests that the deuteration diminishes from the lukewarm and shielded clumps to the warmer and more FUV-irradiated cloud edge.

Table 6. Abundances relative to H_2 in different environments (in units of 10^{-10}).

Molecule	Orion Bar[1*]	Horsehead		Orion KL		L1157-B1[7]	IRAS 16293-2422[8]	B1-b[9]
	PDR	PDR[2*]	Core[3*]	HC[4]	CR[5]	Outflow	Hot corino	Dense core
HCO	1.7	8.4[b]	<0.8[b]	–	<0.3[6,g]	–	<2.0	0.2[n]
HNCO	0.2	–	–	780[h]	–	605[k]	1.7	0.7[p]
H_2CO	9.0	2.9[c]	2.0[c]	1200[h]	440[h]	4000[l]	7.0	4.6[q]
H_2CS	0.8	–	–	150[h]	74[h]	1100[l]	–	0.9[q]
t-HCOOH†	0.2[a]	0.5[d]	0.1[d]	800[i]	–	–	<3.0	0.1[n]
CH_2NH	0.2	–	–	42[h]	–	–	<5.0	–
H_2CCO	0.9	1.5[d]	0.5[d]	–	51[h]	–	1.8	0.2[n]
HC_3N	0.07	0.06[e]	0.08[e]	81[h]	–	100[l]	0.3	3.1[r]
CH_3OH	5.0	1.2[f]	2.3[f]	22 000[h]	12 000[h]	115 000[l]	44	31[r,s]
CH_3CN	0.2	2.5[e]	0.08[e]	300[h]	120[h]	–	1.5	0.4[r]
CH_3CHO	0.8	0.7[d]	0.2[d]	9.5[i]	–	250[m]	1.0	0.1[n]
CH_3CCH	<1.0	4.4[d]	3.0[d]	24[i]	133[6,i]	–	6.5	5.0[r]

Notes. [(*)] A bundances with respect to total hydrogen nuclei. † To date, the cis conformer of HCOOH has only been detected towards the Orion Bar PDR (Cuadrado et al. 2016), therefore, we only provide the abundances of the trans conformer. [(1)] This work. Abundances calculated assuming uniform beam filling. References: [(a)] Cuadrado et al. (2016). [(2)] Low-UV field Horsehead PDR ($\chi \approx 60$; $N_H = 3.8 \times 10^{22}$ cm^{-2}) and [(3)] condensation shielded from the UV field (dense core, $N_H = 6.4 \times 10^{22}$ cm^{-2}) behind the Horsehead PDR edge. Ref.: [(b)] Gerin et al. (2009), [(c)] Guzmán et al. (2011), [(d)] Guzmán et al. (2014), [(e)] Gratier et al. (2013), [(f)] Guzmán et al. (2013). [(4)] Orion KL Hot Core (HC); and [(5)] Orion KL Compact Ridge (CR). [(6)] Abundances calculated for the Extended Ridge. Ref.: [(g)] Blake et al. (1987), [(h)] Crockett et al. (2014), [(i)] B. Tercero, priv. comm.. [(7)] Peak B1 in the blue lobe of the L1157. Ref.: [(k)] Mendoza et al. (2014), [(l)] Bachiller & Pérez Gutiérrez (1997), [(m)] Codella et al. (2015). [(8)] Low-mass protostar (hot corino) IRAS 16293-2422. The abundances are computed for a $N(H_2) = 2 \times 10^{23}$ cm^{-2}. Abundances averaged over a ~20″ beam (van Dishoeck et al. 1995). [(9)] Quiescent dark core Barnard 1-b (B1-b), $N(H_2) = 1.3 \times 10^{23}$ cm^{-2} (see e.g. Hirano et al. 1999; Lis et al. 2002). Ref.: [(n)] Cernicharo et al. (2012), [(p)] Marcelino et al. (2009),[(q)] Marcelino et al. (2005), [(r)] N. Marcelino, priv. comm., [(s)] see also Öberg et al. (2010).

6. Discussion

In order to shed more light on the possible chemical formation routes of COMs in strongly FUV-irradiated gas from an observational perspective, we compare the observed abundances of several COMs and precursors in different environments (see Table 6). In addition to the Orion Bar, we consider the Horsehead PDR (a low-FUV-flux PDR) and a nearby cold core also in the Horsehead nebula, the Orion KL hot core and compact ridge (warm dense gas at roughly the same distance to the Bar), the L1157 outflow (shocked gas), the low-mass protostar IRAS 16293-2422 (hot corino), and the quiescent dark cloud Barnard 1-b (B1-b).

6.1. COMs in different environments

Figure 19 shows a comparison between the abundances of 12 organic molecules detected in the above sources. As expected for widespread interstellar molecules, abundant H_2CO and CH_3OH are found in all sources ($N(X)/N(H_2) > 10^{-10}$). In diffuse and translucent clouds ($n(H_2) \simeq 10^2$–10^3 cm^{-3}), only H_2CO has been detected so far (Liszt et al. 2006), suggesting that the formation of COMs is more efficient in dense gas.

In general, the abundances of COMs, and CH_3OH in particular, are much higher towards Orion KL (hot core and compact ridge) and towards the L1157-B1 outflow. This translates into low $[X_{COM}]/[CH_3OH] \ll 1$ abundance ratios in those environments. The Horsehead PDR, however, shows $[X_{COM}]/[CH_3OH] > 1$ ratios for X_{COM} = HCO, H_2CO, H_2CCO, CH_3CN, and CH_3CCH abundances. The Orion KL hot core and compact ridge show enhanced COM abundances. Owing to the very high dust temperatures ($T_d > 100$ K), ice sublimation and subsequent warm gas-phase chemistry dominates (e.g. Blake et al. 1987). On the other hand, the abundances inferred in the hot corino IRAS 16293-2422 (lower dust temperatures) are more similar to those in the Orion Bar PDR and Horsehead. Interestingly, the L1157 outflow shows the highest abundances of CH_3OH, H_2CO, H_2CS, HC_3N, and CH_3CHO. This suggests that the combined effects of ice mantle sublimation, grain sputtering, and hot gas-phase chemistry in shocks results in a very efficient COM formation.

Among the studied species, only the HCO radical and cis-HCOOH (Cuadrado et al. 2016) are more abundant in PDRs. This enhancement is thus a characteristic feature of FUV-illuminated gas. Figure 20 shows normalised abundances with respect to the abundances in B1-b (cold and gas shielded from strong FUV radiation). HCO, CH_3CHO, H_2CCO, H_2CO, and trans-HCOOH are a factor of ~2–10 more abundant in the PDRs than in the cold core.

Guzmán et al. (2014) observed two positions of the Horsehead, the moderately warm PDR ($T_k \simeq 60$ K) and a cold core behind the PDR and shielded from stellar FUV field. Interestingly, they found enhanced COM abundances in the PDR compared to the core. Given the low-FUV field in the Horsehead, dust grains are relatively cold even at the PDR edge ($T_d \lesssim 30$ K, Goicoechea et al. 2009). These dust temperatures are significantly below the sublimation temperatures of abundant interstellar ices (Gibb et al. 2000) such as H_2O (~100 K), CH_3OH (~100 K), and even H_2CO (~40 K). Hence, grains must be coated with mantles, even in the Horsehead PDR, and photodesorption can be efficient, either desorbing specific COMs or their gas-phase precursors (Guzmán et al. 2014). Indeed, PDR models

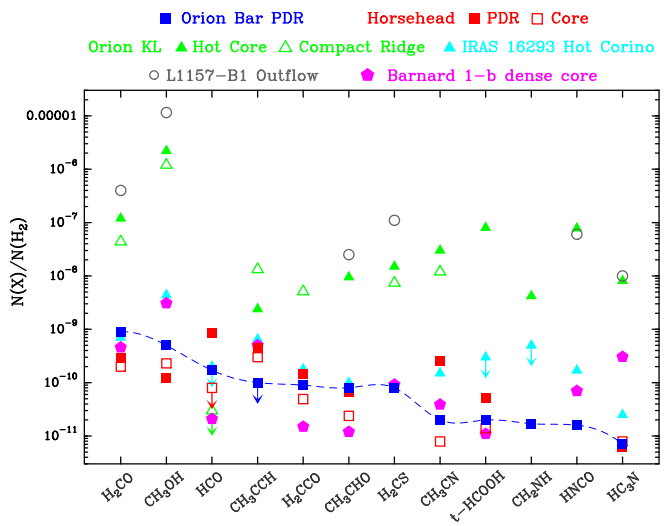

Fig. 19. Molecular abundances with respect to H_2 in several sources. In the Orion Bar PDR, blue points represent the molecular abundance assuming uniform beam filling.

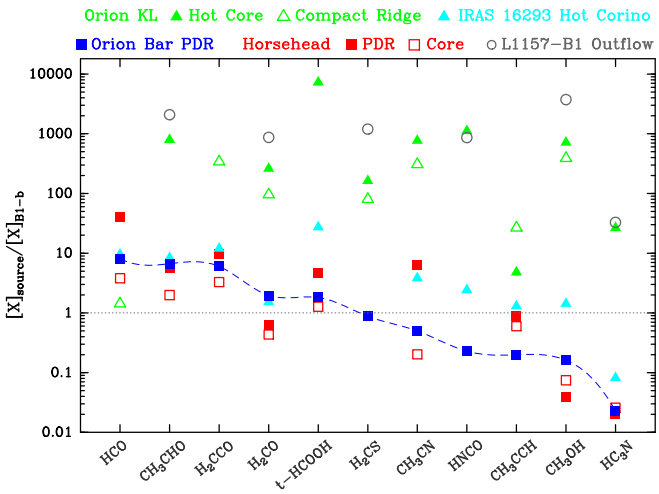

Fig. 20. Comparison of the abundance ratios with respect to B1-b in several sources.

adapted to the Horsehead and including grain surface reactions and ice photodesorption were invoked to explain the observed gas-phase CH_3OH and H_2CO abundances (Guzmán et al. 2013). In addition, the low H_2CO ortho-to-para ratio of two in the PDR (Guzmán et al. 2011) might support a cold surface origin for H_2CO. However, those Horsehead models required relatively high photodesorption yields (several 10^{-4} to 10^{-3} molecules per photon) that are apparently not supported by recent laboratory experiments of methanol photodesorption. In fact, little CH_3OH is actually seen to desorb in CH_3OH ice irradiation experiments (Bertin et al. 2016; Cruz-Diaz et al. 2016).

Also in the Horsehead, CH_3CN is 30 times more abundant in the PDR than in the shielded core (Gratier et al. 2013). CH_3CN is also an order of magnitude more abundant in the Horsehead than in the Orion Bar PDR. Given the high binding energy of CH_3CN ice (similar to CH_3OH, Collings et al. 2004) this result is quite surprising (methanol is more abundant than CH_3CN in the Bar). In addition, Gratier et al. (2013) detected CH_3NC towards the Horsehead PDR, with an isomeric ratio of $[CH_3NC]/[CH_3CN] = 0.15$, higher than our upper limit. These authors suggested that photodesorption triggers the CH_3CN abundance in the Horsehead. Therefore, photodesorption seems to enhance the gas-phase CH_3CN and CH_3NC abundances, but not that of CH_3OH. This suggests that photodesorption is a very selective process and thus, should be studied molecule by molecule in representative ISM ice analogs. In addition, gas phase reactions may allow the enhancement of CH_3CN with respect to CH_3OH.

In the Orion Bar, a much more strongly FUV-irradiated PDR, gas and dust grains are warmer (from $T_d \simeq 40$ to 80 K; Arab et al. 2012). Thus, ice mantle abundances must be small close to the cloud edge. Interestingly, we find higher H_2CO and CH_3OH abundances in the Bar than in the Horsehead PDR (but not HCO). In addition, H_2CO is detected close to the irradiated edge of the Orion Bar and we determine a H_2CO ortho-to-para ratio of approximately three (consistent with the high temperature limit). Finally, we determine a $HCO/H_2CO/CH_3OH \simeq 1/5/3$ abundance ratio, whereas a ~7/2/1 ratio is found in the Horsehead PDR (Gerin et al. 2009; Guzmán et al. 2013). The ratios typically inferred in cold dense gas are ~1/10/10 (Bacmann & Faure 2016). Although HCO is approximately five times more abundant in the Horsehead, both PDRs show $[CH_3OH]/[H_2CO] < 1$ abundance ratios. We note that H_2CO is also a product of photodissociation of CH_3OH. In warm but FUV-shielded environments (hot cores and shocks), CH_3OH is much more abundant than in PDRs and cold cores.

6.2. Limits to steady-state PDR gas-phase chemistry

In order to explore the gas-phase production of HCO, H_2CO, and CH_3OH, we show PDR model results adapted to the illumination conditions in the Bar using the Meudon PDR code (e.g. Le Petit et al. 2006; Goicoechea & Le Bourlot 2007). This is a model of a high gas-pressure isobaric PDR with $\chi = 2 \times 10^4$ and $P_{th}/k = 10^8$ K cm^{-3}. Only H_2O, CO, and atoms are allowed to deplete from the gas following their adsorption energies (e.g. Hollenbach et al. 2009). However, we do not include surface chemistry (e.g. water ice only forms through water vapour freeze-out and desorbs thermally or by photodesorption; we refer to Cuadrado et al. 2015, for details). Figure 21 shows the abundance profiles as a function of cloud depth. Although the dust temperature is never low enough to allow CO ice-mantle formation, water ice starts to be very abundant at $A_V \gtrsim 5$ (a similar behaviour can be expected for CH_3OH ice). We note that the typical gas temperature inferred from our observations towards the line survey position ($T_k \approx 150$ K) corresponds to $A_V \approx 1.5$–2.0 mag and $T_d \approx 60$ K in this model. Hence, we expect mostly bare grains at the edge of the PDR, only coated with a few monolayers of very polar ices such as water (with high adsorption energies).

The model shown in Fig. 21 roughly reproduces the HCO abundance enhancement at the PDR edge (driven by reaction $O + CH_2 \rightarrow HCO + H$), but underpredicts the observed H_2CO and CH_3OH abundances. In these models, the H_2CO formation at $A_V \approx 1.5$–2.0 mag is largely dominated by reaction $O + CH_3 \rightarrow H_2CO + H$. This comparison suggests either the gas-phase model misses important formation routes (or rates) in hot molecular gas, or that (nearly bare) grain surface formation and subsequent desorption is important. Esplugues et al. (2016) have shown PDR models including surface chemistry on grains with different ice content. In their models, chemical/reactive desorption (the surface reaction exothermicity is used to break

the adsorbate-surface bond, e.g. Herbst 2015; Minissale et al. 2016), can dominate over photodesorption for some species (e.g. methanol). Nevertheless, the H_2CO and CH_3OH abundances predicted by Esplugues et al. (2016) in a PDR with high FUV fluxes are still lower than our observed values. Hence, at present, no model seems to reproduce the inferred abundances of molecules such as H_2CO and CH_3OH towards the Bar.

All these models, however, simulate a static PDR in which steady-state has been reached. A real PDR is likely to be more dynamic (Goicoechea et al. 2016). Time-dependent flows of molecular gas and icy grains might advect from inside the cold molecular cloud to the warm PDR edge. There they can be reprocessed by the combination of high temperatures and the presence of a strong FUV photon flux for some time before photodissociation. Thus, time-dependent desorption and advection of COMs (or gas-phase precursors) from the molecular cloud interior to the PDR may contribute to enhance their abundances.

The non-detection of HDCO at the illuminated edge of the Bar ([HDCO]/[H_2CO] $< 3 \times 10^{-3}$), and also in the Horsehead PDR (Guzmán et al. 2011), shows that pure gas-phase H_2CO deuteration is not efficient at high gas temperatures. However, HDCO has been detected towards the lukewarm ($T_k \lesssim 70$ K), dense and more FUV-shielded clump #3 by Parise et al. (2009). This agrees with specific chemical models in which pure gas-phase deuteration is efficient in gas below $T_k \lesssim 70$ K (Roueff et al. 2007). Time-dependent gas-phase models show that the [HDCO]/[H_2CO] abundance ratio is particularly low at early cloud times (Treviño-Morales et al. 2014). In hot cores where high abundances of COMs have been detected, the gas deuteration is very high as well. Both effects are related to the sublimation of ice mantles formed and deuterated in a previous cold cloud stage. In the context of a dynamic PDR, deuterated species could desorb from grain surfaces and advect to the PDR edge as well. The very low [HDCO]/[H_2CO] upper limit abundance towards the edge of the Bar suggests that this mechanism is not efficient for deuterated molecules, and that the gas temperature is too high to enhance the deuterium fractionation by pure gas-phase reactions alone.

6.3. CH_3CCH non detection

CH_3CCH is a widespread hydrocarbon present in the Horsehead PDR ($\sim 4.4 \times 10^{-10}$) and cold core ($\sim 3 \times 10^{-10}$), the extended ridge of Orion KL ($\sim 1 \times 10^{-8}$), the hot corino IRAS 16293-2422 ($\sim 7 \times 10^{-10}$), the Monoceros R2 ultra-compact H II region ($\sim 2 \times 10^{-9}$; Ginard et al. 2012), and even the nucleus of the starburst galaxy M 82 ($\sim 1 \times 10^{-8}$; Fuente et al. 2005; Aladro et al. 2011). Unexpectedly, CH_3CCH lines are not bright towards the Bar edge. A few 2σ line features seen in the 1 mm range coincide with the expected frequencies of CH_3CCH. However, the detection cannot be confirmed with confidence at the sensitivity level of our line survey. Based on the tentative 2σ features, we estimate an upper limit abundance of [CH_3CCH] $< (0.8-1.3) \times 10^{-10}$. The unattenuated CH_3CCH photodissociation rate is high (several 10^{-9} s^{-1} for $\chi = 1$) and CH_3CCH reacts with C^+ ions relatively fast (e.g. Wakelam et al. 2012). Both the FUV photon flux and the C^+ column density are particularly high towards the observed position at the edge of the Bar (Ossenkopf et al. 2013; Goicoechea et al. 2015). This combination likely explains the reduced CH_3CCH abundance. Indeed, in our PDR models, CH_3CCH only reaches detectable abundances at $A_V > 8$ (Cuadrado et al. 2015).

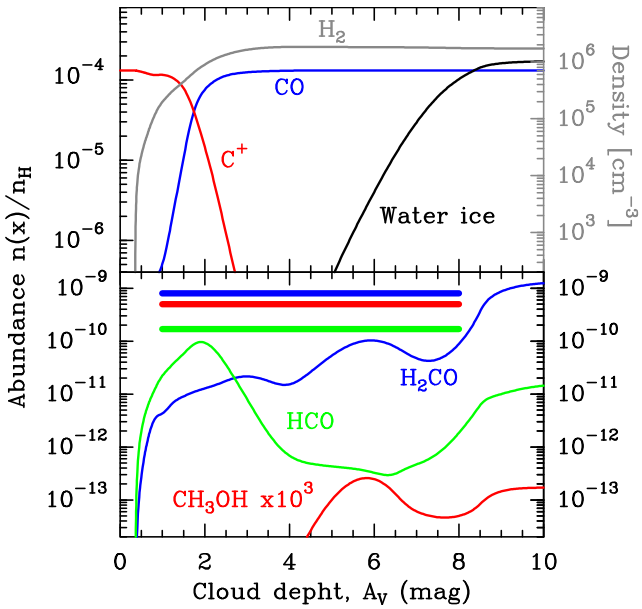

Fig. 21. Isobaric PDR model for the Orion Bar with $P_{th}/k = 10^8$ K cm^{-3} and $\chi = 2 \times 10^4$. The thick horizontal bars show the inferred abundances of HCO, H_2CO, and CH_3OH towards the PDR edge. In this model, these molecules are formed only through gas-phase reactions.

7. Summary and conclusions

We have investigated the presence and abundance of complex organic molecules in the strongly FUV-irradiated edge of the Orion Bar PDR, near the H_2 dissociation front. We used the IRAM 30 m telescope to carry out a millimetre line survey, complemented with 8.5″ resolution maps of the molecular line emission at 0.9 mm. Despite being a very harsh environment, our observations show a relatively rich spectrum, with more than 250 lines arising from COMs and related organic precursors with up to seven atoms: H_2CO, CH_3OH, HCO, H_2CCO, CH_3CHO, H_2CS, HCOOH, CH_3CN, CH_2NH, HNCO, $H_2^{13}CO$, and HC_3N (in decreasing order of abundance). In particular, we obtained the following results:

- The abundance of the detected species range from 10^{-9} to 10^{-11}; H_2CO being the most abundant. The inferred rotational temperatures range from ~10 to ~55 K, significantly lower than the gas temperature and thus consistent with subthermal excitation. $H_2^{13}CO$ and H_2CCO have the lowest and the highest rotational temperatures, respectively. We obtain similar rotational temperatures for the ortho-para and A-E species, and ortho-to-para ratios of approximately three.
- For some molecules, we constrain the beam-averaged physical conditions from LVG excitation models. As shown by previous works (e.g. Leurini et al. 2006, 2010), we conclude that not all COMs arise from the same PDR layer. In particular, while CH_3OH only arises from dense gas in the more shielded PDR interior ($T_k = 40-50$ K), CH_3CN and H_2CO also trace warmer gas layers ($T_k = 150-250$ K), more exposed to a strong FUV-field.
- We determine a HCO/H_2CO/CH_3OH $\simeq$ 1/5/3 abundance ratio. Such relative abundances are not inferred in environments dominated by ice-mantle thermal desorption or grain sputtering. Overall, pure gas-phase models have difficulty reproducing the observed H_2CO and especially CH_3OH abundances in PDRs. Taking into account the elevated gas and dust temperatures at the edge of the Bar ($T_d \simeq 60$ K),

we suggest the following scenarios for the formation of COMs: (i) hot gas reactions not included in current models; (ii) COMs are produced in the warm grain surfaces of nearly bare grains; or (iii) the PDR dynamics is such that COMs or specific precursors formed in cold icy grains deeper inside the molecular cloud desorb and advect into the PDR.

The presence of COMs in the interstellar medium is more widespread that initially expected. It includes very harsh environments such as shocked gas and now strongly FUV-irradiated gas. COM formation reflects the complicated interplay between gas and grain surface chemistry in different environments. However, the specific formation pathways are not fully clear and may even not be the same in different environments. More laboratory experiments to study different grain surface processes and to investigate the products and rates of different desorption mechanisms (photodesorption, sublimation, chemical desorption, etc.) are needed to distinguish between the different possible scenarios. The census of increasingly complex organic molecule detections will obviously increase in the years to come.

Acknowledgements. We thank our referee for pointing us towards several missing references in an earlier version of the manuscript. We thank Nuria Marcelino for sharing the column densities of different COMs inferred towards Barnard 1-b. We are very grateful to the IRAM staff for their help during the observations. This work has been partially funded by MINECO grants (CSD2009-00038 and AYA2012-32032). We thank the ERC for support under grant ERC-2013-Syg-610256-NANOCOSMOS.

References

Agúndez, M., Cernicharo, J., & Goicoechea, J. R. 2008, A&A, 483, 831
Aladro, R., Martín, S., Martín-Pintado, J., et al. 2011, A&A, 535, A84
Allegrini, M., Johns, J. W. C., & McKellar, A. R. W. 1979, J. Chem. Phys., 70, 2829
Andree-Labsch, S., Ossenkopf-Okada, V., & Röllig, M. 2017, A&A, 598, A2
Anttila, R., Horneman, V. M., Koivusaari, M., & Paso, R. 1993, J. Mol. Spectr., 157, 198
Arab, H., Abergel, A., Habart, E., et al. 2012, A&A, 541, A19
Austin, J. A., Levy, D. H., Gottlieb, C. A., & Radford, H. E. 1974, J. Chem. Phys., 60, 207
Avery, L. W., Broten, N. W., MacLeod, J. M., Oka, T., & Kroto, H. W. 1976, ApJ, 205, L173
Bachiller, R., & Pérez Gutiérrez, M. 1997, ApJ, 487, L93
Bacmann, A., & Faure, A. 2016, A&A, 587, A130
Bacmann, A., Taquet, V., Faure, A., Kahane, C., & Ceccarelli, C. 2012, A&A, 541, L12
Batrla, W., & Wilson, T. L. 2003, A&A, 408, 231
Beers, Y., Klein, G. P., Kirchhoff, W. H., & Johnson, D. R. 1972, J. Mol. Spectr., 44, 553
Belloche, A., Garrod, R. T., Müller, H. S. P., et al. 2009, A&A, 499, 215
Belloche, A., Garrod, R. T., Müller, H. S. P., & Menten, K. M. 2014, Science, 345, 1584
Bertin, M., Romanzin, C., Doronin, M., et al. 2016, ApJ, 817, L12
Bisschop, S. E., Jørgensen, J. K., van Dishoeck, E. F., & de Wachter, E. B. M. 2007, A&A, 465, 913
Blake, G. A., Sastry, K. V. L. N., & de Lucia, F. C. 1984, J. Chem. Phys., 80, 95
Blake, G. A., Sutton, E. C., Masson, C. R., & Phillips, T. G. 1987, ApJ, 315, 621
Bockelée-Morvan, D., Crovisier, J., Mumma, M. J., & Weaver, H. A. 2004, The composition of cometary volatiles, Comets II (University of Arizona Press), 391
Bocquet, R., Demaison, J., Poteau, L., et al. 1996, J. Mol. Spectr., 177, 154
Bottinelli, S., Ceccarelli, C., Lefloch, B., et al. 2004, ApJ, 615, 354
Boucher, D., Burie, J., Demaison, J., et al. 1977, J. Mol. Spectr., 64, 290
Bowater, I. C., Brown, J. M., & Carrington, A. 1971, J. Chem. Phys., 54, 4957
Brown, R. D., Crofts, J. G., Godfrey, P. D., et al. 1975, ApJ, 197, L29
Brown, R. D., Godfrey, P. D., McNaughton, D., Pierlot, A. P., & Taylor, W. H. 1990, J. Mol. Spectr., 140, 340
Brünken, S., Müller, H. S. P., Lewen, F., & Winnewisser, G. 2003, Phys. Chem. Chem. Phys. (Incorporating Faraday Transactions), 5
Burton, M. G., Hollenbach, D. J., & Tielens, A. G. G. M. 1990, ApJ, 365, 620
Caselli, P., & Ceccarelli, C. 2012, A&ARv, 20, 56
Cazaux, S., Tielens, A. G. G. M., Ceccarelli, C., et al. 2003, ApJ, 593, L51
Cazzoli, G., & Puzzarini, C. 2006, J. Mol. Spectr., 240, 153
Cernicharo, J. 2012, in EAS Pub. Ser., 58, 251
Cernicharo, J., Bachiller, R., & Duvert, G. 1986, A&A, 160, 181
Cernicharo, J., Guélin, M., & Kahane, C. 2000, A&AS, 142, 181
Cernicharo, J., Heras, A. M., Tielens, A. G. G. M., et al. 2001, ApJ, 546, L123
Cernicharo, J., Marcelino, N., Roueff, E., et al. 2012, ApJ, 759, L43
Cernicharo, J., Kisiel, Z., Tercero, B., et al. 2016, A&A, 587, L4
Chen, W., Bocquet, R., Wlodarczak, G., & Boucher, D. 1991, International Journal of Infrared and Millimeter Waves, 12, 987
Codella, C., Fontani, F., Ceccarelli, C., et al. 2015, MNRAS, 449, L11
Collings, M. P., Anderson, M. A., Chen, R., et al. 2004, MNRAS, 354, 1133
Creswell, R. A., Winnewisser, G., & Gerry, M. C. L. 1977, J. Mol. Spectr., 65, 420
Crockett, N. R., Bergin, E. A., Neill, J. L., et al. 2014, ApJ, 787, 112
Cronin, J. R., & Chang, S. 1993, in NATO Advanced Science Institutes (ASI) Series C, eds. J. M. Greenberg, C. X. Mendoza-Gómez, & V. Pirronello, 416, 209
Cruz-Diaz, G. A., Muñoz Caro, G. M., Martín-Doménech, R., & Chen, Y.-J. 2016, A&A, 592, A68
Cuadrado, S., Goicoechea, J. R., Pilleri, P., et al. 2015, A&A, 575, A82
Cuadrado, S., Goicoechea, J. R., Roncero, O., et al. 2016, A&A, 596, L1
DeLeon, R. L., & Muenter, J. S. 1985, J. Chem. Phys., 82, 1702
de Zafra, R. L. 1971, ApJ, 170, 165
Dickinson, D. F. 1972, Astrophys. Lett., 12, 235
Dore, L., Bizzocchi, L., Degli Esposti, C., & Gauss, J. 2010, J. Mol. Spectr., 263, 44
Dore, L., Bizzocchi, L., & Degli Esposti, C. 2012, A&A, 544, A19
Draine, B. T., Roberge, W. G., & Dalgarno, A. 1983, ApJ, 264, 485
Eliet, S., Cuisset, A., Guinet, M., et al. 2012, J. Mol. Spectr., 279, 12
Esplugues, G. B., Cazaux, S., Meijerink, R., Spaans, M., & Caselli, P. 2016, A&A, 591, A52
Fabricant, B., Krieger, D., & Muenter, J. S. 1977, J. Chem. Phys., 67, 1576
Fuente, A., García-Burillo, S., Gerin, M., et al. 2005, ApJ, 619, L155
Fuente, A., García-Burillo, S., Usero, A., et al. 2008, A&A, 492, 675
Gadhi, J., Lahrouni, A., Legrand, J., & Demaison, J. 1995, J. Chim. Phys., 92, 1984
Gerin, M., Goicoechea, J. R., Pety, J., & Hily-Blant, P. 2009, A&A, 494, 977
Gibb, E. L., Whittet, D. C. B., Schutte, W. A., et al. 2000, ApJ, 536, 347
Ginard, D., González-García, M., Fuente, A., et al. 2012, A&A, 543, A27
Goicoechea, J. R., & Le Bourlot, J. 2007, A&A, 467, 1
Goicoechea, J. R., Compiègne, M., & Habart, E. 2009, ApJ, 699, L165
Goicoechea, J. R., Joblin, C., Contursi, A., et al. 2011, A&A, 530, L16
Goicoechea, J. R., Teyssier, D., Etxaluze, M., et al. 2015, ApJ, 812, 75
Goicoechea, J. R., Pety, J., Cuadrado, S., et al. 2016, Nature, 537, 207
Goicoechea, J. R., Cuadrado, S., Pety, J., et al. 2017, A&A, 601, L9
Goldsmith, P. F., & Langer, W. D. 1999, ApJ, 517, 209
Gottlieb, C. A. 1973, in Molecules in the Galactic Environment, eds. M. A. Gordon, & L. E. Snyder, 181
Gratier, P., Pety, J., Guzmán, V., et al. 2013, A&A, 557, A101
Green, S. 1986, ApJ, 309, 331
Green, S. 1991, ApJS, 76, 979
Greve, A., Kramer, C., & Wild, W. 1998, A&AS, 133, 271
Guzmán, V., Pety, J., Goicoechea, J. R., Gerin, M., & Roueff, E. 2011, A&A, 534, A49
Guzmán, V. V., Goicoechea, J. R., Pety, J., et al. 2013, A&A, 560, A73
Guzmán, V. V., Pety, J., Gratier, P., et al. 2014, Faraday Discussions, 168, 103
Guzmán, V. V., Pety, J., Goicoechea, J. R., et al. 2015, ApJ, 800, L33
Habart, E., Dartois, E., Abergel, A., et al. 2010, A&A, 518, L116
Herbst, E. 2015, in EPJ Web Conf., 84, 06002
Herbst, E., & van Dishoeck, E. F. 2009, ARA&A, 47, 427
Hirano, N., Kamazaki, T., Mikami, H., Ohashi, N., & Umemoto, T. 1999, in Star Formation 1999, ed. T. Nakamoto, 181
Hocking, W. H., Gerry, M. C. L., & Winnewisser, G. 1975, Can. J. Phys., 53, 1869
Hogerheijde, M. R., Jansen, D. J., & van Dishoeck, E. F. 1995, A&A, 294, 792
Hollenbach, D., Kaufman, M. J., Bergin, E. A., & Melnick, G. J. 2009, ApJ, 690, 1497
Ikeda, M., Ohishi, M., Nummelin, A., et al. 2001, ApJ, 560, 792
Jansen, D. J., Spaans, M., Hogerheijde, M. R., & van Dishoeck, E. F. 1995, A&A, 303, 541
Johns, J. W. C., Nemes, L., Yamada, K. M. T., et al. 1992, J. Mol. Spectr., 156, 501
Johnson, H. R., & Strandberg, M. W. P. 1952, J. Chem. Phys., 20, 687
Johnson, D. R., Powell, F. X., & Kirchhoff, W. H. 1971, J. Mol. Spectr., 39, 136
Kirchhoff, W. H., Johnson, D. R., & Lovas, F. J. 1973, J. Phys. Chem. Ref. Data, 2, 1
Kleiner, I., Lovas, F. J., & Godefroid, M. 1996, J. Phys. Chem. Ref. Data, 25, 1113

Kukolich, S. G. 1982, J. Chem. Phys., 76, 97
Kukolich, S., Nelson, A., & Yamanashi, B. 1971, J. Am. Chem. Soc., 93, 6769
Kukolich, S. G., Ruben, D. J., Wang, J. H. S., & Williams, J. R. 1973, J. Chem. Phys., 58, 3155
Langer, W. D., & Penzias, A. A. 1990, ApJ, 357, 477
Lapinov, A. V., Golubiatnikov, G. Y., Markov, V. N., & Guarnieri, A. 2007, Astron. Lett., 33, 121
Le Petit, F., Nehmé, C., Le Bourlot, J., & Roueff, E. 2006, ApJS, 164, 506
Lees, R. M., & Baker, J. G. 1968, J. Chem. Phys., 48, 5299
Lees, R. M., Lovas, F. J., Kirchhoff, W. H., & Johnson, D. R. 1973, J. Phys. Chem. Ref. Data, 2, 205
Leurini, S., Rolffs, R., Thorwirth, S., et al. 2006, A&A, 454, L47
Leurini, S., Parise, B., Schilke, P., Pety, J., & Rolffs, R. 2010, A&A, 511, A82
Lis, D. C., & Schilke, P. 2003, ApJ, 597, L145
Lis, D. C., Roueff, E., Gerin, M., et al. 2002, ApJ, 571, L55
Liszt, H. S., Lucas, R., & Pety, J. 2006, A&A, 448, 253
Maeda, A., Medvedev, I. R., Winnewisser, M., et al. 2008, ApJS, 176, 543
Marcelino, N., Cernicharo, J., Roueff, E., Gerin, M., & Mauersberger, R. 2005, ApJ, 620, 308
Marcelino, N., Cernicharo, J., Tercero, B., & Roueff, E. 2009, ApJ, 690, L27
Marconi, A., Testi, L., Natta, A., & Walmsley, C. M. 1998, A&A, 330, 696
Mbosei, L., Fayt, A., Dréan, P., & Cosléou, J. 2000, J. Mol. Structure, 517, 271
Meier, D. S., & Turner, J. L. 2005, ApJ, 618, 259
Meier, D. S., & Turner, J. L. 2012, ApJ, 755, 104
Mendoza, E., Lefloch, B., López-Sepulcre, A., et al. 2014, MNRAS, 445, 151
Menten, K. M., Reid, M. J., Forbrich, J., & Brunthaler, A. 2007, A&A, 474, 515
Minissale, M., Moudens, A., Baouche, S., Chaabouni, H., & Dulieu, F. 2016, MNRAS, 458, 2953
Müller, H. S. P., Gendriesch, R., Margulès, L., et al. 2000, Phys. Chem. Chem. Phys. (Incorporating Faraday Transactions), 2
Müller, H. S. P., Thorwirth, S., Roth, D. A., & Winnewisser, G. 2001, A&A, 370, L49
Müller, H. S. P., Schlöder, F., Stutzki, J., & Winnewisser, G. 2005, J. Mol. Structure, 742, 215
Müller, H. S. P., Drouin, B. J., & Pearson, J. C. 2009, A&A, 506, 1487
Nagy, Z., Van der Tak, F. F. S., Ossenkopf, V., et al. 2013, A&A, 550, A96
Nagy, Z., Choi, Y., Ossenkopf-Okada, V., et al. 2017, A&A, 599, A22
Öberg, K. I., Bottinelli, S., Jørgensen, J. K., & van Dishoeck, E. F. 2010, ApJ, 716, 825
Ossenkopf, V., Röllig, M., Neufeld, D. A., et al. 2013, A&A, 550, A57
Parise, B., Leurini, S., Schilke, P., et al. 2009, A&A, 508, 737
Parmar, P. S., Lacy, J. H., & Achtermann, J. M. 1991, ApJ, 372, L25
Pavone, F. S., Zink, L. R., Prevedelli, M., Inguscio, M., & Fusina, L. 1990, J. Mol. Spectr., 144, 45
Pickett, H. M., Poynter, R. L., Cohen, E. A., et al. 1998, J. Quant. Spectr. Rad. Transf., 60, 883
Rabli, D., & Flower, D. R. 2010, MNRAS, 406, 95
Remijan, A. J., Hollis, J. M., Snyder, L. E., Jewell, P. R., & Lovas, F. J. 2006, ApJ, 643, L37
Requena-Torres, M. A., Martín-Pintado, J., Rodríguez-Franco, A., et al. 2006, A&A, 455, 971
Roueff, E., Parise, B., & Herbst, E. 2007, A&A, 464, 245
Saito, S. 1972, ApJ, 178, L95
Sastry, K. V. L. N., Lees, R. M., & Van der Linde, J. 1981, J. Mol. Spectr., 88, 228
Schilke, P., Pineau des Forêts, G., Walmsley, C. M., & Martín-Pintado, J. 2001, A&A, 372, 291
Simon, R., Stutzki, J., Sternberg, A., & Winnewisser, G. 1997, A&A, 327, L9
Snyder, L. E., Buhl, D., Zuckerman, B., & Palmer, P. 1969, Phys. Rev. Lett., 22, 679
Stoerzer, H., Stutzki, J., & Sternberg, A. 1995, A&A, 296, L9
Tercero, B., Cernicharo, J., Pardo, J. R., & Goicoechea, J. R. 2010, A&A, 517, A96
Tercero, B., Kleiner, I., Cernicharo, J., et al. 2013, ApJ, 770, L13
Tercero, B., Cernicharo, J., López, A., et al. 2015, A&A, 582, L1
Thorwirth, S., Müller, H. S. P., & Winnewisser, G. 2000, J. Mol. Spectr., 204, 133
Tielens, A. G. G. M., & Hollenbach, D. 1985a, ApJ, 291, 747
Tielens, A. G. G. M., & Hollenbach, D. 1985b, ApJ, 291, 722
Tielens, A. G. G. M., Meixner, M. M., van der Werf, P. P., et al. 1993, Science, 262, 86
Treviño-Morales, S. P., Pilleri, P., Fuente, A., et al. 2014, A&A, 569, A19
Turner, B. E. 1971, ApJ, 163, L35
Šimečková, M., Urban, Š., Fuchs, U., et al. 2004, J. Mol. Spectr., 226, 123
van der Tak, F. F. S., Nagy, Z., Ossenkopf, V., et al. 2013, A&A, 560, A95
van der Werf, P. P., Stutzki, J., Sternberg, A., & Krabbe, A. 1996, A&A, 313, 633
van der Werf, P. P., Goss, W. M., & O'Dell, C. R. 2013, ApJ, 762, 101
van der Wiel, M. H. D., van der Tak, F. F. S., Ossenkopf, V., et al. 2009, A&A, 498, 161
van Dishoeck, E. F., Blake, G. A., Jansen, D. J., & Groesbeck, T. D. 1995, ApJ, 447, 760
Wakelam, V., Herbst, E., Loison, J.-C., et al. 2012, ApJS, 199, 21
Walmsley, C. M., Natta, A., Oliva, E., & Testi, L. 2000, A&A, 364, 301
Wernli, M., Wiesenfeld, L., Faure, A., & Valiron, P. 2007, A&A, 464, 1147
Wilson, T. L., & Rood, R. 1994, ARA&A, 32, 191
Xu, L.-H., Fisher, J., Lees, R. M., et al. 2008, J. Mol. Spectr., 251, 305
Yamada, K. M. T., Moravec, A., & Winnewisser, G. 1995, Zeitschrift Naturforschung Teil A, 50, 1179
Young Owl, R. C., Meixner, M. M., Wolfire, M., Tielens, A. G. G. M., & Tauber, J. 2000, ApJ, 540, 886
Ziurys, L. M., & McGonagle, D. 1993, ApJS, 89, 155

Appendix A: Possible line emission contamination from the telescope side lobes

In order to determine whether or not the emission from the bright Orion BN/KL region contributes to our detected signal, we compared the 1 mm spectrum of the Orion Bar with that of Orion BN/KL (located at ~2′ north of the Bar, e.g. Tercero et al. 2010). Figure A.1 shows several H_2CS and CH_3OH lines observed towards the Bar (black histogram) and Orion BN/KL (red histogram; see Tercero et al. 2010, 2015). We note that the amplitude of Orion BN/KL spectra are divided by a given value to match the line intensities from the Bar. This comparison shows that while the line emission from the Orion Bar peaks at $v_{LSR} \simeq 10.7$ km s^{-1}, and can be fully attributed to gas in the PDR (Goicoechea et al. 2016), the blue-shifted shoulder emission seen in some lines at ~8 km s^{-1} is likely produced by the intense emission from Orion BN/KL, and perhaps by the extended Orion cloud component (for the low-excitation lines). This emission is detected through the telescope extended side lobes and results in a blue-shifted emission shoulder in some spectra towards the Bar. For the IRAM 30 m telescope, the contribution of the secondary lobes increases with frequency (Greve et al. 1998). Given the specific emission velocity and narrow line widths of the emission from the Bar, and the fact that this effect is stronger at ~1 mm, we conclude that our line assignments and line intensity extraction in the PDR is correct.

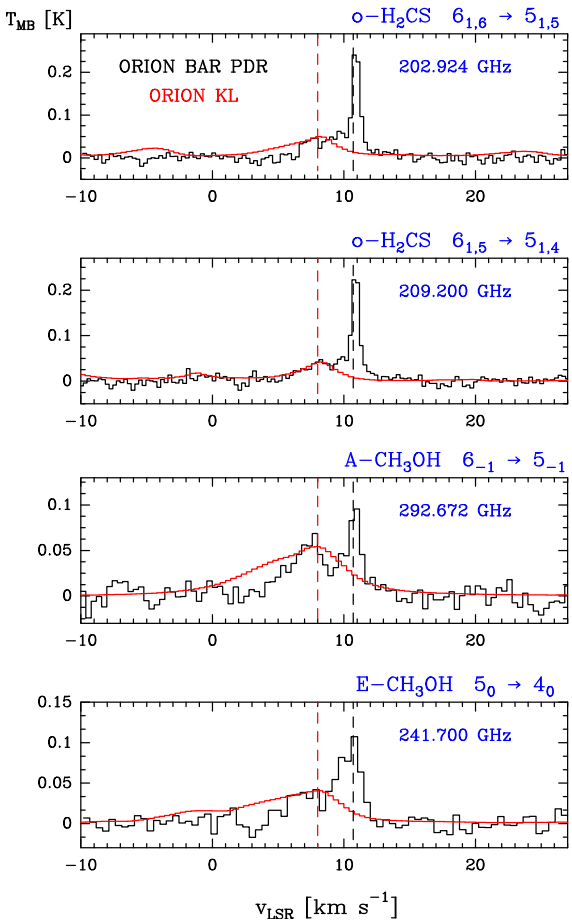

Fig. A.1. Orion Bar spectra (black) at different frequencies in the 1 mm range. For each line, the spectrum towards Orion BN/KL is also shown in red (Tercero et al. 2010, 2015). The CH_3OH spectra towards Orion BN/KL have been divided by ~400, and the H_2CS spectra by ~200. The black and red dashed lines indicate the LSR velocity of the Orion Bar PDR (10.7 km s^{-1}) and Orion extended ridge and/or south hot core (~8 km s^{-1}, see e.g. Cernicharo et al. 2016), respectively.

Appendix B: Identified lines of complex organic molecules

A summary of the main line spectroscopic parameters is presented in Tables B.1–B.11. Line frequency (in MHz), energy of the upper level of each transition (E_u/k in K), Einstein coefficient for spontaneous emission (A_{ul} in s^{-1}), intrinsic line strength (S_{ul}), and the level degeneracy (g_u) from MADEX spectral catalogue, and JPL and CDMS molecular databases are shown. The velocity-integrated line intensity ($\int T_{MB} dv$ in mK km s^{-1}), LSR velocity (v_{LSR} in km s^{-1}), FWHM line width (Δv in km s^{-1}), and the line peak temperature (T_{MB} in mK) were obtained from Gaussian fits. Parentheses indicate the uncertainty. When two or more transitions were found to overlap, the total profile was fitted. Fully overlapping transitions are marked with connecting symbols in the tables.

Table B.1. Line parameters of HCO.

Transition	Frequency	E_u/k	A_{ul}	S_{ul}	g_u	$\int T_{MB} dv$	v_{LSR}	Δv	T_{MB}	S/N
$(N_{K_a,K_c}, J, F)_u \rightarrow (N_{K_a,K_c}, J, F)_l$	[MHz]	[K]	[s^{-1}]			[mK km s^{-1}]	[km s^{-1}]	[km s^{-1}]	[mK]	
$1_{0,1}$, 3/2, 2 → $0_{0,0}$, 1/2, 1	86 670.760^F	4.2	4.68×10^{-6}	1.66	5	497(12)	10.5(<0.1)	3.1(0.1)	149	52
$1_{0,1}$, 3/2, 1 → $0_{0,0}$, 1/2, 0	86 708.360^F	4.2	4.59×10^{-6}	0.98	3	286(7)	10.5(<0.1)	2.8(0.1)	95	33
$1_{0,1}$, 1/2, 1 → $0_{0,0}$, 1/2, 1	86 777.460^F	4.2	4.60×10^{-6}	0.98	3	294(7)	10.5(<0.1)	3.0(0.1)	92	32
$1_{0,1}$, 1/2, 0 → $0_{0,0}$, 1/2, 1	86 805.780^F	4.2	4.71×10^{-6}	0.33	1	75(6)	10.5(0.1)	2.3(0.2)	31	10
$2_{0,2}$, 5/2, 3 → $1_{0,1}$, 3/2, 2	173 377.377^W	12.5	4.50×10^{-5}	2.80	7	683(86)	–	–	–	8
$2_{0,2}$, 5/2, 2 → $1_{0,1}$, 3/2, 1	173 406.082^W	12.5	4.42×10^{-5}	1.96	5	346(70)	–	–	–	6
$2_{0,2}$, 3/2, 2 → $1_{0,1}$, 1/2, 1	173 443.065^W	12.5	3.38×10^{-5}	1.50	5	409(94)	–	–	–	5
$2_{0,2}$, 3/2, 1 → $1_{0,1}$, 1/2, 0	173 474.400^W	12.5	2.50×10^{-5}	0.66	3	185(79)	–	–	–	4
$3_{0,3}$, 7/2, 4 → $2_{0,2}$, 5/2, 3	260 060.329^F	25.0	1.63×10^{-4}	3.85	9	576(15)	10.5(<0.1)	2.0(0.1)	275	23
$3_{0,3}$, 7/2, 3 → $2_{0,2}$, 5/2, 2	260 082.192^F	25.0	1.60×10^{-4}	2.95	7	446(15)	10.5(<0.1)	2.0(0.1)	209	16
$3_{0,3}$, 5/2, 3 → $2_{0,2}$, 3/2, 2	260 133.586^F	25.0	1.45×10^{-4}	2.67	7	347(17)	10.6(<0.1)	1.7(0.4)	195	15
$3_{0,3}$, 5/2, 2 → $2_{0,2}$, 3/2, 1	260 155.769^W	25.0	1.37×10^{-4}	1.80	5	382(25)	–	–	–	19
$4_{0,4}$, 9/2, 5 → $3_{0,3}$, 7/2, 4	346 708.493^F	41.6	3.99×10^{-4}	4.88	11	437(38)	10.6(0.1)	2.6(0.3)	156	7
$4_{0,4}$, 9/2, 4 → $3_{0,3}$, 7/2, 3	346 725.172^F	41.6	3.95×10^{-4}	3.95	9	308(36)	10.6(0.1)	2.0(0.3)	142	7
$4_{0,4}$, 7/2, 4 → $3_{0,3}$, 5/2, 3	346 787.898^F	41.6	3.76×10^{-4}	3.76	9	362(41)	10.5(0.2)	3.0(0.5)	112	6
$4_{0,4}$, 7/2, 3 → $3_{0,3}$, 5/2, 2	346 804.597^F	41.6	3.67×10^{-4}	2.85	7	223(29)	10.6(0.1)	1.6(0.3)	127	7

Notes. Frequencies, E_u/k, A_{ul}, S_{ul}, and g_u from JPL catalogue. Labels: $^{(F)}$ Detected with FTS backend. $^{(W)}$ The lines detected with WILMA backend just give information about the integrated line intensity (see Cuadrado et al. 2015). $^{(*)}$ Symmetry (ortho-para or E-A).

Table B.2. Line parameters of H_2CO.

Transition	Sym.*	Frequency	E_u/k	A_{ul}	S_{ul}	g_u	$\int T_{MB} dv$	v_{LSR}	Δv	T_{MB}	S/N
$(J_{K_a,K_c})_u \rightarrow (J_{K_a,K_c})_l$		[MHz]	[K]	[s^{-1}]			[mK km s^{-1}]	[km s^{-1}]	[km s^{-1}]	[mK]	
$2_{1,2} \rightarrow 1_{1,1}$	*ortho*	$140\,839.516^W$	6.8	5.30×10^{-5}	1.5	5	13488(28)	–	–	–	423
$2_{0,2} \rightarrow 1_{0,1}$	*para*	$145\,602.951^W$	10.5	7.80×10^{-5}	2.0	5	5611(67)	–	–	–	95
$2_{1,1} \rightarrow 1_{1,0}$	*ortho*	$150\,498.335^W$	7.5	6.46×10^{-5}	1.5	5	10 850(97)	–	–	–	208
$3_{1,3} \rightarrow 2_{1,2}$	*ortho*	$211\,211.449^F$	16.9	2.27×10^{-4}	2.7	7	13 732(26)	10.6(0.1)	2.3(0.1)	5519	338
$3_{0,3} \rightarrow 2_{0,2}$	*para*	$218\,222.187^F$	21.0	2.81×10^{-4}	3.0	7	6567(22)	10.6(0.1)	2.2(0.1)	2771	311
$3_{2,2} \rightarrow 2_{2,1}$	*para*	$218\,475.634^F$	68.1	1.57×10^{-4}	1.7	7	2600(9)	10.7(0.1)	2.1(0.1)	1148	175
$3_{2,1} \rightarrow 2_{2,0}$	*para*	$218\,760.062^F$	68.1	1.58×10^{-4}	1.7	7	2582(12)	10.7(0.1)	2.1(0.1)	1145	151
$3_{1,2} \rightarrow 2_{1,1}$	*ortho*	$225\,697.772^F$	18.3	2.77×10^{-4}	2.7	7	11 382(39)	10.6(0.1)	2.4(0.1)	4537	269
$4_{1,4} \rightarrow 3_{1,3}$	*ortho*	$281\,526.919^F$	30.4	5.87×10^{-4}	3.8	9	15 275(49)	10.5(0.1)	2.4(0.1)	6032	409
$4_{2,3} \rightarrow 3_{2,2}$	*para*	$291\,237.765^F$	82.1	5.20×10^{-4}	3.0	9	2870(19)	10.6(0.1)	2.1(0.1)	1266	100
$4_{3,2} \rightarrow 3_{3,1}$	*ortho*	$291\,380.441^F$	125.8	3.04×10^{-4}	1.8	9	3815(19)	10.6(0.1)	2.0(0.1)	1755	138
$4_{3,1} \rightarrow 3_{3,0}$	*ortho*	$291\,384.360^F$	125.8	3.04×10^{-4}	1.8	9	4282(21)	10.7(0.1)	2.3(0.1)	1744	138
$4_{2,2} \rightarrow 3_{2,1}$	*para*	$291\,948.066^F$	82.1	5.24×10^{-4}	3.0	9	2863(19)	10.6(0.1)	2.2(0.1)	1244	101
$4_{1,3} \rightarrow 3_{1,2}$	*ortho*	$300\,836.630^F$	32.7	7.17×10^{-4}	3.8	9	9897(49)	10.7(0.1)	2.5(0.1)	3668	135
$5_{1,5} \rightarrow 4_{1,4}$	*ortho*	$351\,768.637^F$	47.3	1.20×10^{-3}	4.8	11	8551(88)	10.7(0.1)	2.4(0.1)	3294	61

Notes. Frequencies, E_u/k, A_{ul}, S_{ul}, and g_u from MADEX code, that fit to all rotational lines reported by Bocquet et al. (1996), Brünken et al. (2003), and Eliet et al. (2012).

Table B.3. Line parameters of $H_2^{13}CO$.

Transition	Sym.*	Frequency	E_u/k	A_{ul}	S_{ul}	g_u	$\int T_{MB} dv$	v_{LSR}	Δv	T_{MB}	S/N
$(J_{K_a,K_c})_u \rightarrow (J_{K_a,K_c})_l$		[MHz]	[K]	[s^{-1}]			[mK km s^{-1}]	[km s^{-1}]	[km s^{-1}]	[mK]	
$2_{1,2} \rightarrow 1_{1,1}$	*ortho*	$137\,449.954^W$	6.6	4.92×10^{-5}	1.5	5	298(53)	–	–	–	7
$2_{1,1} \rightarrow 1_{1,0}$	*ortho*	$146\,635.669^W$	7.3	5.98×10^{-5}	1.5	5	73(29)	–	–	–	5
$3_{1,3} \rightarrow 2_{1,2}$	*ortho*	$206\,131.619^F$	16.5	2.11×10^{-4}	2.6	7	251(12)	10.5(0.1)	2.4(0.1)	97	11
$3_{0,3} \rightarrow 2_{0,2}$	*para*	$212\,811.190^F$	20.4	2.61×10^{-4}	3.0	7	84(13)	10.3(0.1)	2.1(0.4)	37	4
$3_{1,2} \rightarrow 2_{1,1}$	*ortho*	$219\,908.481^F$	17.8	2.56×10^{-4}	2.7	7	151(12)	10.7(0.1)	2.0(0.2)	70	7
$4_{1,4} \rightarrow 3_{1,3}$	*ortho*	$274\,762.103^F$	29.7	5.46×10^{-4}	3.8	9	180(16)	10.8(0.1)	2.3(0.3)	74	6
$4_{0,4} \rightarrow 3_{0,3}$	*para*	$283\,441.868^F$	34.0	6.39×10^{-4}	4.0	9	32(13)	10.7(0.2)	0.9(0.5)	33	4
$4_{1,3} \rightarrow 3_{1,2}$	*ortho*	$293\,126.495^F$	31.9	6.63×10^{-4}	3.8	9	140(13)	10.5(0.1)	2.3(0.3)	58	6

Notes. Frequencies, E_u/k, A_{ul}, S_{ul}, and g_u from MADEX code, that fit to all rotational lines reported by Müller et al. (2000).

Table B.4. Line parameters of H_2CS.

Transition	Sym.*	Frequency	E_u/k	A_{ul}	S_{ul}	g_u	$\int T_{MB} dv$	v_{LSR}	Δv	T_{MB}	S/N
$(J_{K_a,K_c})_u \rightarrow (J_{K_a,K_c})_l$		[MHz]	[K]	[s^{-1}]			[mK km s^{-1}]	[km s^{-1}]	[km s^{-1}]	[mK]	
$3_{1,3} \rightarrow 2_{1,2}$	*ortho*	$101\,477.810^F$	8.1	1.26×10^{-5}	2.67	7	79(8)	10.8(0.1)	1.1(0.1)	68	10
$3_{2,2} \rightarrow 2_{2,1}$	*para*	$103\,039.907^F$	62.6	8.25×10^{-6}	1.67	7	⟩ 53(5)	10.9(0.1)	1.8(0.2)	28	9
$3_{0,3} \rightarrow 2_{0,2}$	*para*	$103\,040.452^F$	9.9	1.48×10^{-5}	3.00	7					
$3_{2,1} \rightarrow 2_{2,0}$	*para*	$103\,051.847^F$	62.6	8.25×10^{-6}	1.67	7	19(7)	10.5(0.3)	1.5(1.3)	10	3
$3_{1,2} \rightarrow 2_{1,1}$	*ortho*	$104\,617.040^F$	8.4	1.38×10^{-5}	2.67	7	85(5)	10.7(<0.1)	1.3(0.1)	59	14
$4_{0,4} \rightarrow 3_{0,3}$	*para*	$137\,371.210^W$	16.5	3.65×10^{-5}	4.00	9	182(18)	–	–	–	2
$4_{1,3} \rightarrow 3_{1,2}$	*ortho*	$139\,483.682^W$	15.1	3.58×10^{-5}	3.75	9	149(22)	–	–	–	4
$5_{1,5} \rightarrow 4_{1,4}$	*ortho*	$169\,114.079^W$	22.7	6.68×10^{-5}	4.80	11	229(35)	–	–	–	10
$5_{0,5} \rightarrow 4_{0,4}$	*para*	$171\,688.117^W$	24.7	7.28×10^{-5}	5.00	11	1447(217)	–	–	–	9
$5_{1,4} \rightarrow 4_{1,3}$	*ortho*	$174\,345.223^W$	23.5	7.32×10^{-5}	4.80	11	300(106)	–	–	–	3
$6_{1,6} \rightarrow 5_{1,5}$	*ortho*	$202\,924.054^F$	32.5	1.19×10^{-4}	5.83	13	206(10)	10.9(<0.1)	0.8(0.1)	245	18
$6_{0,6} \rightarrow 5_{0,5}$	*para*	$205\,987.858^F$	34.6	1.28×10^{-4}	6.00	13	75(7)	10.9(<0.1)	0.7(0.1)	104	10
$6_{3,4} \rightarrow 5_{3,3}$	*ortho*	$206\,052.602^F$	138.3	9.59×10^{-5}	4.50	13	⟩ 76(14)	10.9(0.1)	1.3(0.4)	55	5
$6_{3,3} \rightarrow 5_{3,2}$	*ortho*	$206\,052.602^F$	138.3	9.59×10^{-5}	4.50	13					
$6_{2,4} \rightarrow 5_{2,3}$	*para*	$206\,158.602^F$	87.3	1.14×10^{-4}	5.33	13	48(7)	10.9(0.1)	1.0(0.1)	47	5
$6_{1,5} \rightarrow 5_{1,4}$	*ortho*	$209\,200.620^F$	33.5	1.30×10^{-4}	5.83	13	190(9)	10.9(<0.1)	0.8(0.1)	231	17
$7_{1,7} \rightarrow 6_{1,6}$	*ortho*	$236\,727.020^F$	43.8	1.92×10^{-4}	6.86	15	105(14)	10.9(<0.1)	0.5(0.1)	185	7
$7_{0,7} \rightarrow 6_{0,6}$	*para*	$240\,266.872^F$	46.1	2.05×10^{-4}	7.00	15	107(13)	10.8(<0.1)	0.9(0.1)	116	8
$7_{2,6} \rightarrow 6_{2,5}$	*para*	$240\,382.051^F$	98.8	1.88×10^{-4}	6.43	15	24(6)	10.8(0.1)	0.3(0.2)	76	3
$7_{3,5} \rightarrow 6_{3,4}$	*ortho*	$240\,393.037^F$	149.8	1.68×10^{-4}	5.71	15	⟩ 122(14)	10.5(0.1)	1.6(0.2)	72	6
$7_{3,4} \rightarrow 6_{3,3}$	*ortho*	$240\,393.762^F$	149.8	1.68×10^{-4}	5.71	15					
$7_{2,5} \rightarrow 6_{2,4}$	*para*	$240\,549.066^F$	98.8	1.89×10^{-4}	6.43	15	62(11)	10.7(0.1)	1.5(0.2)	54	5
$7_{1,6} \rightarrow 6_{1,5}$	*ortho*	$244\,048.504^F$	45.2	2.10×10^{-4}	6.86	15	185(11)	10.9(<0.1)	0.8(0.1)	260	14
$8_{1,8} \rightarrow 7_{1,7}$	*ortho*	$270\,521.931^F$	56.8	2.90×10^{-4}	7.88	17	128(16)	10.8(0.1)	0.9(0.2)	139	6
$8_{0,8} \rightarrow 7_{0,7}$	*para*	$274\,521.931^F$	59.3	3.08×10^{-4}	8.00	17	60(9)	11.1(0.1)	0.7(0.1)	77	5
$8_{2,6} \rightarrow 7_{2,5}$	*para*	$274\,953.744^F$	112.0	2.90×10^{-4}	7.50	17	36(9)	11.0(0.1)	0.9(0.2)	39	3
$8_{1,7} \rightarrow 7_{1,6}$	*ortho*	$278\,887.661^F$	58.6	3.18×10^{-4}	7.87	17	195(13)	10.9(<0.1)	0.7(0.1)	245	14
$9_{1,9} \rightarrow 8_{1,8}$	*ortho*	$304\,307.709^F$	71.4	4.17×10^{-4}	8.89	19	75(8)	10.7(0.1)	0.7(0.1)	101	5
$10_{1,10} \rightarrow 9_{1,9}$	*ortho*	$338\,083.195^F$	87.6	5.77×10^{-4}	9.90	21	108(30)	10.6(0.1)	0.9(0.3)	113	3

Notes. Frequencies, E_u/k, A_{ul}, S_{ul}, and g_u from CDMS catalogue.

Table B.5. Line parameters of HNCO.

Transition	Frequency	E_u/k	A_{ul}	S_{ul}	g_u	$\int T_{MB} dv$	v_{LSR}	Δv	T_{MB}	S/N
$(J_{K_a,K_c})_u \rightarrow (J_{K_a,K_c})_l$	[MHz]	[K]	[s^{-1}]			[mK km s^{-1}]	[km s^{-1}]	[km s^{-1}]	[mK]	
$4_{0,4} \rightarrow 3_{0,3}$	$87\,925.237^F$	10.5	9.03×10^{-6}	4.0	9	49(6)	10.8(0.1)	1.7(0.2)	27	8
$5_{0,5} \rightarrow 4_{0,4}$	$109\,905.749^F$	15.8	1.80×10^{-5}	5.0	11	110(9)	10.6(0.1)	1.9(0.2)	54	10
$7_{0,7} \rightarrow 6_{0,6}$	$153\,865.086^W$	29.5	5.08×10^{-5}	7.0	15	125(39)	–	–	–	3
$10_{0,10} \rightarrow 9_{0,9}$	$219\,798.274^F$	58.0	1.51×10^{-4}	10.0	21	154(16)	10.6(0.2)	3.3(0.4)	44	6
$11_{0,11} \rightarrow 10_{0,10}$	$241\,774.032^F$	69.6	2.02×10^{-4}	11.0	23	118(21)	10.7(0.1)	1.6(0.3)	69	5
$13_{0,13} \rightarrow 12_{0,12}$	$285\,721.951^F$	96.0	3.36×10^{-4}	13.0	27	129(26)	10.4(0.3)	2.8(0.7)	43	5

Notes. Frequencies, E_u/k, A_{ul}, S_{ul}, and g_u from CDMS catalogue.

Table B.6. Line parameters of CH_2NH.

Transition	Frequency	E_u/k	A_{ul}	S_{ul}	g_u	$\int T_{MB} dv$	v_{LSR}	Δv	T_{MB}	S/N
$(J_{K_a,K_c})_u \rightarrow (J_{K_a,K_c})_l$	[MHz]	[K]	[s^{-1}]			[mK km s^{-1}]	[km s^{-1}]	[km s^{-1}]	[mK]	
$4_{0,4} \rightarrow 3_{1,3}$	$105\,794.062^F$	30.6	1.62×10^{-5}	5.0	9	55(13)	11.3(0.5)	4.2(1.3)	12	3
$1_{1,1} \rightarrow 0_{0,0}$	$225\,554.609^F$	10.8	2.79×10^{-4}	3.0	3	120(26)	10.5(0.2)	2.9(0.9)	39	4
$4_{1,4} \rightarrow 3_{1,3}$	$245\,125.866^F$	37.3	3.85×10^{-4}	11.2	9	106(14)	11.1(0.1)	2.3(0.4)	43	4
$6_{0,6} \rightarrow 5_{1,5}$	$251\,421.265^F$	64.1	2.73×10^{-4}	9.2	13	72(13)	11.0(0.3)	3.1(0.6)	22	4
$4_{0,4} \rightarrow 3_{0,3}$	$254\,685.137^F$	30.6	4.60×10^{-4}	12.0	9	314(12)	10.8(0.1)	2.0(0.1)	147	14
$4_{1,3} \rightarrow 3_{1,2}$	$266\,270.024^F$	39.8	4.93×10^{-4}	11.2	9	117(12)	10.9(0.1)	2.0(0.2)	54	5

Notes. Frequencies, E_u/k, A_{ul}, S_{ul}, and g_u from CDMS catalogue.

Table B.7. Line parameters of H_2CCO.

Transition	Sym.*	Frequency	E_u/k	A_{ul}	S_{ul}	g_u	$\int T_{MB}\,dv$	v_{LSR}	Δv	T_{MB}	S/N
$(J_{K_a,K_c})_u \rightarrow (J_{K_a,K_c})_l$		[MHz]	[K]	[s^{-1}]			[mK km s^{-1}]	[km s^{-1}]	[km s^{-1}]	[mK]	
$4_{2,3} \rightarrow 3_{2,2}$	*para*	80 820.400^F	61.9	4.14×10^{-6}	3.0	9	13(9)	10.9(0.7)	1.6(0.7)	8	2
$4_{1,3} \rightarrow 3_{1,2}$	*ortho*	81 586.239^F	8.8	5.33×10^{-6}	3.8	9	44(8)	11.0(0.3)	2.5(0.6)	13	4
$5_{1,5} \rightarrow 4_{1,4}$	*ortho*	100 094.511^F	13.5	1.03×10^{-5}	4.8	11	61(6)	10.4(0.2)	1.9(0.5)	30	3
$5_{3,3} \rightarrow 4_{3,2}$	*ortho*	101 002.349^F	117.9	7.06×10^{-6}	3.2	11	⟩ 25(8)	10.3(0.2)	1.0(0.3)	25	3
$5_{3,2} \rightarrow 4_{3,1}$	*ortho*	101 002.354^F	117.9	7.06×10^{-6}	3.2	11					
$5_{2,4} \rightarrow 4_{2,3}$	*para*	101 024.430^F	66.7	9.27×10^{-6}	4.2	11	24(6)	10.2(0.2)	1.7(0.8)	15	2
$5_{1,4} \rightarrow 4_{1,3}$	*ortho*	101 981.442^F	13.7	1.09×10^{-5}	4.8	11	58(6)	10.9(0.1)	2.3(0.3)	24	7
$7_{1,7} \rightarrow 6_{1,6}$	*ortho*	140 127.471^W	25.9	2.96×10^{-5}	6.9	15	107(43)	–	–	–	5
$7_{3,5} \rightarrow 6_{3,4}$	*ortho*	141 402.460^W	130.5	2.54×10^{-5}	5.7	15	⟩ 71(32)	–	–	–	4
$7_{3,4} \rightarrow 6_{3,3}$	*ortho*	141 402.491^W	130.5	2.54×10^{-5}	5.7	15					
$8_{1,7} \rightarrow 7_{1,6}$	*ortho*	163 160.893^W	34.3	4.74×10^{-5}	7.9	17	114(22)	–	–	–	5
$11_{1,11} \rightarrow 10_{1,10}$	*ortho*	220 177.558^F	62.4	1.19×10^{-4}	10.9	23	128(13)	10.8(0.1)	2.6(0.3)	47	5
$11_{3,9} \rightarrow 10_{3,8}$	*ortho*	222 199.879^F	167.4	1.14×10^{-4}	10.2	23	⟩ 120(13)	10.5(0.1)	1.9(0.5)	59	8
$11_{3,8} \rightarrow 10_{3,7}$	*ortho*	222 200.199^F	167.4	1.14×10^{-4}	10.2	23					
$11_{2,10} \rightarrow 10_{2,9}$	*para*	222 228.629^F	116.2	1.20×10^{-4}	10.6	23	54(15)	10.7(0.1)	2.0(0.8)	25	4
$11_{1,10} \rightarrow 10_{1,9}$	*ortho*	224 327.246^F	63.6	1.26×10^{-4}	10.9	23	125(11)	10.8(0.1)	2.5(0.2)	47	7
$12_{1,12} \rightarrow 11_{1,11}$	*ortho*	240 185.798^F	74.0	1.56×10^{-4}	11.9	25	123(19)	10.9(0.2)	2.6(0.6)	45	5
$12_{0,12} \rightarrow 11_{0,11}$	*para*	242 375.721^F	75.6	1.61×10^{-4}	12.0	25	38(11)	10.5(0.1)	0.8(0.2)	46	2
$12_{1,11} \rightarrow 11_{1,10}$	*ortho*	244 712.254^F	75.4	1.64×10^{-4}	11.9	25	123(13)	10.8(0.1)	1.7(0.1)	69	5
$13_{1,13} \rightarrow 12_{1,12}$	*ortho*	260 191.993^W	86.5	1.99×10^{-4}	12.9	27	100(19)	–	–	–	7
$13_{0,13} \rightarrow 12_{0,12}$	*para*	262 548.202^F	88.2	2.05×10^{-4}	13.0	27	35(9)	10.8(0.1)	1.2(0.2)	28	3
$13_{3,11} \rightarrow 12_{3,10}$	*ortho*	262 596.638^F	191.6	1.94×10^{-4}	12.3	27	⟩ 108(17)	10.7(0.1)	2.1(0.3)	46	5
$13_{3,10} \rightarrow 12_{3,9}$	*ortho*	262 597.384^F	191.6	1.94×10^{-4}	12.3	27					
$13_{2,12} \rightarrow 12_{2,11}$	*para*	262 618.994^F	140.4	2.00×10^{-4}	12.7	27	43(9)	10.7(0.2)	1.5(0.2)	27	3
$13_{2,11} \rightarrow 12_{2,10}$	*para*	262 760.857^F	140.5	2.01×10^{-4}	12.7	27	38(15)	10.3(0.3)	1.8(0.8)	20	3
$13_{1,12} \rightarrow 12_{1,11}$	*ortho*	265 095.061^F	88.1	2.10×10^{-4}	13.0	27	99(10)	10.7(0.1)	1.5(0.1)	63	6
$14_{1,14} \rightarrow 13_{1,13}$	*ortho*	280 195.979^F	99.9	2.49×10^{-4}	13.9	29	128(13)	10.6(0.1)	2.0(0.2)	61	6
$14_{0,14} \rightarrow 13_{0,13}$	*para*	282 714.584^F	101.8	2.57×10^{-4}	14.0	29	33(15)	10.8(0.3)	1.0(0.3)	31	3
$14_{3,12} \rightarrow 13_{3,11}$	*ortho*	282 794.399^F	205.2	2.45×10^{-4}	13.4	29	⟩ 131(15)	10.5(0.1)	2.0(0.2)	62	6
$14_{3,11} \rightarrow 13_{3,10}$	*ortho*	282 795.485^F	205.2	2.45×10^{-4}	13.4	29					
$14_{2,13} \rightarrow 13_{2,12}$	*para*	282 811.466^F	154.0	2.52×10^{-4}	13.7	29	39(13)	10.5(0.1)	0.9(0.3)	45	4
$14_{2,12} \rightarrow 13_{2,11}$	*para*	282 988.739^F	154.0	2.52×10^{-4}	13.7	29	34(7)	10.7(0.1)	1.0(0.2)	34	4
$14_{1,13} \rightarrow 13_{1,12}$	*ortho*	285 475.477^F	101.8	2.63×10^{-4}	13.9	29	107(18)	10.5(0.2)	1.8(0.3)	54	4
$15_{1,15} \rightarrow 14_{1,14}$	*ortho*	300 197.596^F	114.3	3.07×10^{-4}	14.9	31	89(39)	10.7(0.4)	1.9(0.5)	44	2
$15_{3,13} \rightarrow 14_{3,12}$	*ortho*	302 991.695^F	219.7	3.04×10^{-4}	14.4	31	⟩ 116(28)	11.0(0.3)	2.2(0.4)	49	2
$15_{3,12} \rightarrow 14_{3,11}$	*ortho*	302 993.234^F	219.7	3.04×10^{-4}	14.4	31					

Notes. Frequencies, E_u/k, A_{ul}, S_{ul}, and g_u from MADEX code, that fit to all rotational lines reported in the CDMS database.

Table B.8. Line parameters of HC_3N.

Transition	Frequency	E_u/k	A_{ul}	S_{ul}	g_u	$\int T_{MB} dv$	v_{LSR}	Δv	T_{MB}	S/N
$J_u \rightarrow J_l$	[MHz]	[K]	[s^{-1}]			[mK km s^{-1}]	[km s^{-1}]	[km s^{-1}]	[mK]	
$9 \rightarrow 8$	$81\,881.462^F$	19.6	4.22×10^{-5}	9.0	19	50(19)	10.8(0.2)	2.1(0.6)	23(s)	6
$10 \rightarrow 9$	$90\,978.989^F$	24.0	5.81×10^{-5}	10.0	21	86(11)	10.5(0.2)	2.9(0.4)	28	6
$11 \rightarrow 10$	$100\,076.385^F$	28.8	7.77×10^{-5}	11.0	23	80(14)	10.5(0.2)	1.8(0.3)	42	6
$12 \rightarrow 11$	$109\,173.637^F$	34.1	1.01×10^{-4}	12.0	25	76(8)	10.7(0.1)	2.0(0.2)	37	10
$15 \rightarrow 14$	$136\,464.402^W$	52.4	1.99×10^{-4}	15.0	31	164(59)	–	–	–	3
$16 \rightarrow 15$	$145\,560.949^W$	59.4	2.42×10^{-4}	16.0	33	95(59)	–	–	–	4
$17 \rightarrow 16$	$154\,657.288^W$	66.8	2.91×10^{-4}	17.0	35	162(36)	–	–	–	5
$18 \rightarrow 17$	$163\,753.404^W$	74.7	3.46×10^{-4}	18.0	37	162(20)	–	–	–	8
$19 \rightarrow 18$	$172\,849.285^W$	83.0	4.08×10^{-4}	19.0	39	169(17)	–	–	–	2
$23 \rightarrow 22$	$209\,230.199^F$	120.5	7.27×10^{-4}	23.0	47	54(16)	10.8(0.2)	1.7(0.6)	30	5
$24 \rightarrow 23$	$218\,324.709^F$	131.0	8.26×10^{-4}	24.0	49	16(4)	10.9(0.1)	0.6(0.2)	24	4

Notes. Frequencies, E_u/k, A_{ul}, S_{ul}, and g_u from MADEX code, that fit to all rotational lines reported by de Zafra (1971), Mbosei et al. (2000), Creswell et al. (1977), Chen et al. (1991), Yamada et al. (1995), Thorwirth et al. (2000).

Table B.9. Line parameters of CH_3CN.

Transition	Sym.*	Frequency	E_u/k	A_{ul}	S_{ul}	g_u	$\int T_{MB} dv$	v_{LSR}	Δv	T_{MB}	S/N
$(J_K)_u \rightarrow (J_K)_l$		[MHz]	[K]	[s^{-1}]			[mK km s^{-1}]	[km s^{-1}]	[km s^{-1}]	[mK]	
$5_4 \rightarrow 4_4$	E	$91\,958.726^F$	119.5	2.28×10^{-5}	1.8	11	26(13)	12.5(0.5)	2.0(1.0)	13	3
$5_3 \rightarrow 4_3$	A	$91\,971.130^F$	77.5	4.06×10^{-5}	6.4	22	103(9)	10.2(0.2)	4.0(0.4)	24	6
$5_2 \rightarrow 4_2$	E	$91\,979.993^F$	33.8	5.33×10^{-5}	4.2	11	84(16)	10.6(0.3)	3.0(0.7)	26	6
$5_1 \rightarrow 4_1$	E	$91\,985.313^F$	12.4	6.09×10^{-5}	4.8	11	114(12)	10.5(0.1)	2.6(0.4)	40	9
$5_0 \rightarrow 4_0$	A	$91\,987.087^F$	13.2	6.35×10^{-5}	5.0	11	138(13)	10.9(0.1)	2.8(0.4)	46	11
$6_3 \rightarrow 5_3$	A	$110\,364.353^F$	82.8	8.35×10^{-5}	9.0	26	151(11)	10.8(0.1)	2.7(0.2)	53	8
$6_2 \rightarrow 5_2$	E	$110\,374.988^F$	39.1	9.89×10^{-5}	5.3	13	87(10)	10.7(0.1)	2.0(0.3)	40	7
$6_1 \rightarrow 5_1$	E	$110\,381.371^F$	17.7	1.08×10^{-4}	5.8	13	144(10)	10.8(0.1)	2.1(0.2)	65	10
$6_0 \rightarrow 5_0$	A	$110\,383.499^F$	18.5	1.11×10^{-4}	6.0	13	137(10)	10.8(0.1)	2.1(0.2)	62	11
$7_4 \rightarrow 6_4$	E	$128\,739.669^W$	131.0	1.20×10^{-4}	4.7	15	75(49)	–	–	–	2
$7_3 \rightarrow 6_3$	A	$128\,757.029^W$	89.0	1.46×10^{-4}	11.4	30	181(59)	–	–	–	3
$7_2 \rightarrow 6_2$	E	$128\,769.435^W$	45.3	1.64×10^{-4}	6.4	15	112(62)	–	–	–	4
$7_1 \rightarrow 6_1$	E	$128\,776.880^W$	23.8	1.75×10^{-4}	6.8	15	$\rangle$ 425(59)	–	–	–	6
$7_0 \rightarrow 6_0$	A	$128\,779.363^W$	24.7	1.79×10^{-4}	7.0	15					
$8_3 \rightarrow 7_3$	A	$147\,149.068^W$	96.1	2.31×10^{-4}	13.8	34	149(31)	–	–	–	4
$8_2 \rightarrow 7_2$	E	$147\,163.243^W$	52.3	2.52×10^{-4}	7.5	17	98(33)	–	–	–	2
$8_1 \rightarrow 7_1$	E	$147\,171.751^W$	30.9	2.65×10^{-4}	7.9	17	$\rangle$ 385(41)	–	–	–	8
$8_0 \rightarrow 7_0$	A	$147\,174.587^W$	31.8	2.69×10^{-4}	8.0	17					
$9_4 \rightarrow 8_4$	E	$165\,518.064^W$	146.0	3.09×10^{-4}	7.2	19	85(23)	–	–	–	3
$9_3 \rightarrow 8_3$	A	$165\,540.376^W$	104.0	3.43×10^{-4}	16.0	38	177(20)	–	–	–	9

Table B.9. continued

Transition	Sym.*	Frequency	E_u/k	A_{ul}	S_{ul}	g_u	$\int T_{MB} dv$	v_{LSR}	Δv	T_{MB}	S/N
$(J_K)_u \rightarrow (J_K)_l$		[MHz]	[K]	[s^{-1}]			[mK km s^{-1}]	[km s^{-1}]	[km s^{-1}]	[mK]	
$9_2 \rightarrow 8_2$	E	165 556.321^W	60.3	3.66×10^{-4}	8.6	19	108(19)	–	–	–	7
$9_1 \rightarrow 8_1$	E	165 565.890^W	38.8	3.81×10^{-4}	8.9	19	419(24)	–	–	–	14
$9_0 \rightarrow 8_0$	A	165 569.080^W	39.7	3.86×10^{-4}	9.0	19					
$11_3 \rightarrow 10_3$	A	202 320.442^F	122.6	6.58×10^{-4}	20.3	46	140(11)	10.7(0.1)	2.0(0.2)	64	8
$11_2 \rightarrow 10_2$	E	202 339.920^F	78.8	6.87×10^{-4}	10.6	23	78(9)	10.7(0.1)	1.5(0.2)	49	6
$11_1 \rightarrow 10_1$	E	202 351.610^F	57.4	7.05×10^{-4}	10.9	23	103(13)	10.7(0.2)	2.9(0.4)	33	5
$11_0 \rightarrow 10_0$	A	202 355.507^F	58.3	7.11×10^{-4}	11.0	23	135(11)	10.7(0.1)	2.3(0.2)	55	7
$12_4 \rightarrow 11_4$	E	220 679.287^F	175.1	8.22×10^{-4}	10.7	25	44(12)	10.9(0.3)	1.8(0.5)	23	4
$12_3 \rightarrow 11_3$	A	220 709.016^F	133.2	8.68×10^{-4}	22.5	50	100(15)	10.7(0.1)	1.8(0.4)	52	8
$12_2 \rightarrow 11_2$	E	220 730.259^F	89.4	9.00×10^{-4}	11.7	25	61(15)	10.6(0.3)	1.7(0.0)	34	6
$12_1 \rightarrow 11_1$	E	220 743.009^F	68.0	9.20×10^{-4}	11.9	25	122(15)	10.4(0.1)	1.7(0.2)	72	11
$12_0 \rightarrow 11_0$	A	220 747.259^F	68.9	9.26×10^{-4}	12.0	25	69(15)	10.9(0.2)	1.7(0.3)	38	6
$13_3 \rightarrow 12_3$	A	239 096.495^F	144.6	1.12×10^{-3}	24.6	54	94(16)	10.8(0.1)	1.9(0.5)	46	7
$13_2 \rightarrow 12_2$	E	239 119.503^F	100.9	1.15×10^{-3}	12.7	27	20(11)	10.6(0.3)	1.0(0.8)	19	3
$13_0 \rightarrow 12_0$	A	239 137.914^F	80.3	1.18×10^{-3}	13.0	27	52(9)	10.5(0.2)	1.3(0.4)	23	3
$14_4 \rightarrow 13_4$	E	257 448.128^F	199.0	1.36×10^{-3}	12.9	29	29(10)	10.6(0.3)	1.5(0.6)	19	3
$14_3 \rightarrow 13_3$	A	257 482.790^F	157.0	1.41×10^{-3}	26.7	58	57(17)	10.6(0.2)	1.5(0.3)	36	5
$14_2 \rightarrow 13_2$	E	257 507.560^F	113.3	1.45×10^{-3}	13.7	29	55(10)	10.7(0.1)	1.3(0.3)	40	6
$14_1 \rightarrow 13_1$	E	257522.425^F	91.8	1.47×10^{-3}	13.9	29	53(11)	10.8(0.3)	2.0(0.5)	24	4
$14_0 \rightarrow 13_0$	A	257 527.381^F	92.7	1.48×10^{-3}	14.0	29	42(8)	10.9(0.1)	1.0(0.2)	38	5
$15_3 \rightarrow 14_3$	A	275 867.809^F	170.2	1.75×10^{-3}	28.8	62	61(14)	10.5(0.2)	1.5(0.4)	38	4
$15_2 \rightarrow 14_2$	E	275 894.339^F	126.5	1.79×10^{-3}	14.7	31	31(9)	10.3(0.1)	0.7(0.3)	40	2
$15_1 \rightarrow 14_1$	E	275 910.261^F	105.1	1.81×10^{-3}	14.9	31	30(12)	10.7(0.2)	0.7(0.2)	40	2
$16_3 \rightarrow 15_3$	A	294 251.460^F	184.4	2.14×10^{-3}	30.9	66	55(13)	10.1(0.2)	1.2(0.2)	43	4
$16_2 \rightarrow 15_2$	E	294 279.748^F	140.6	2.18×10^{-3}	15.7	33	33(15)	10.4(0.2)	0.9(0.3)	34	4
$16_1 \rightarrow 15_1$	E	294 296.726^F	119.2	2.21×10^{-3}	15.9	33	34(9)	10.2(0.1)	1.0(0.2)	32	4
$16_0 \rightarrow 15_0$	A	294 302.386^F	120.1	2.22×10^{-3}	16.0	33	27(9)	10.9(0.2)	0.8(0.2)	32	2

Notes. Frequencies, E_u/k, A_{ul}, S_{ul}, and g_u from MADEX code, that fit to all rotational lines reported by Kukolich et al. (1973), Boucher et al. (1977), Kukolich (1982), Pavone et al. (1990), Cazzoli & Puzzarini (2006), Šimečková et al. (2004), Müller et al. (2009).

Table B.10. Line parameters of CH_3OH.

Transition	Sym.*	Frequency	E_u/k	A_{ul}	S_{ul}	g_u	$\int T_{MB} dv$	v_{LSR}	Δv	T_{MB}	S/N
$(J_K)_u \rightarrow (J_K)_l$		[MHz]	[K]	[s^{-1}]			[mK km s^{-1}]	[km s^{-1}]	[km s^{-1}]	[mK]	
$5_{-1} \rightarrow 4_0$	E	84 521.172^F	32.5	1.97×10^{-6}	1.5	11	149(8)	10.6(0.1)	1.6(0.1)	86	18
$8_0 \rightarrow 7_1$	A	95 169.391^F	83.5	2.13×10^{-6}	1.8	17	59(6)	10.4(0.1)	1.5(0.1)	54	14
$2_1 \rightarrow 1_1$	A	95 914.310^F	21.4	2.49×10^{-6}	1.5	5	28(12)	10.8(0.3)	1.7(0.7)	15	2
$2_{-1} \rightarrow 1_{-1}$	E	96 739.358^F	4.6	2.56×10^{-6}	1.5	5	107(9)	10.7(0.1)	1.5(0.1)	67	9
$2_0 \rightarrow 1_0$	A	96 741.371^F	7.0	3.41×10^{-6}	2.0	5	206(9)	10.8(0.1)	1.7(0.2)	114	16
$2_0 \rightarrow 1_0$	E	96 744.545^F	12.2	3.41×10^{-6}	2.0	5	95(12)	10.7(0.1)	1.9(0.3)	44	6
$2_1 \rightarrow 1_1$	E	96 755.501^F	20.1	2.62×10^{-6}	1.5	5	66(13)	10.8(0.2)	2.0(0.5)	27	4
$2_{-1} \rightarrow 1_{-1}$	A	97 582.798^F	21.6	2.63×10^{-6}	1.5	5	32(12)	10.5(0.2)	1.7(0.6)	18	4
$3_1 \rightarrow 4_0$	A	107 013.831^F	28.3	3.07×10^{-6}	0.7	7	30(12)	9.7(0.4)	2.2(0.2)	13	3
$0_0 \rightarrow 1_{-1}$	E	108 893.945^F	5.2	1.47×10^{-5}	0.5	1	45(6)	10.7(0.1)	1.6(0.2)	26	7
$6_{-1} \rightarrow 5_0$	E	132 890.759^W	46.4	7.75×10^{-6}	1.8	13	191(31)	–	–	–	5
$3_1 \rightarrow 2_1$	A	143 865.795^W	28.3	1.07×10^{-5}	2.7	7	74(28)	–	–	–	3
$3_{-1} \rightarrow 2_{-1}$	E	145 097.435^W	11.6	1.10×10^{-5}	2.7	7	269(28)	–	–	–	10
$3_0 \rightarrow 2_0$	A	145 103.185^W	13.9	1.23×10^{-5}	3.0	7	384(83)	–	–	–	12
$3_{-2} \rightarrow 2_{-2}$	A	145 124.332^W	51.6	6.89×10^{-6}	1.7	7					
$3_2 \rightarrow 2_2$	E	145 126.191^W	28.3	6.77×10^{-6}	1.7	7	⟩ 103(23)	–	–	–	4
$3_{-2} \rightarrow 2_{-2}$	E	145 126.386^W	31.9	6.86×10^{-6}	1.7	7					
$3_1 \rightarrow 2_1$	E	145 131.864^W	27.1	1.13×10^{-5}	2.8	7	⟩ 139(24)	–	–	–	5
$3_2 \rightarrow 2_2$	A	145 133.415^W	51.6	6.89×10^{-6}	1.7	7					
$3_{-1} \rightarrow 2_{-1}$	A	146 368.328^W	28.6	1.13×10^{-5}	2.7	7	74(41)	–	–	–	3
$9_0 \rightarrow 8_1$	A	146 618.697^W	104.4	8.04×10^{-6}	2.1	19	92(26)	–	–	–	3
$6_2 \rightarrow 7_1$	A	156 127.544^W	86.5	6.74×10^{-6}	1.0	13	82(30)	–	–	–	3
$2_1 \rightarrow 3_0$	A	156 602.395^W	21.4	8.93×10^{-6}	0.5	5	149(35)	–	–	–	4
$7_0 \rightarrow 7_{-1}$	E	156 828.517^W	70.2	1.88×10^{-5}	3.1	15	61(17)	–	–	–	2
$6_0 \rightarrow 6_{-1}$	E	157 048.617^W	54.0	1.96×10^{-5}	2.8	13	82(27)	–	–	–	3
$1_0 \rightarrow 1_{-1}$	E	157 270.832^W	7.5	2.21×10^{-5}	0.7	3					
$3_0 \rightarrow 3_{-1}$	E	157 272.338^W	19.2	2.15×10^{-5}	1.7	7	⟩ 355(53)	–	–	–	8
$2_0 \rightarrow 2_{-1}$	E	157 276.019^W	12.2	2.18×10^{-5}	1.2	5					
$1_1 \rightarrow 1_0$	E	165 050.175^W	15.5	2.35×10^{-5}	0.7	3	56(22)	–	–	–	2
$2_1 \rightarrow 2_0$	E	165 061.130^W	20.1	2.34×10^{-5}	1.1	5	232(38)	–	–	–	4
$3_1 \rightarrow 3_0$	E	165 099.240^W	27.1	2.33×10^{-5}	1.6	7	170(28)	–	–	–	6
$4_1 \rightarrow 4_0$	E	165 190.475^W	36.4	2.32×10^{-5}	2.0	9	178(70)	–	–	–	6
$5_1 \rightarrow 5_0$	E	165 369.341^W	48.0	2.31×10^{-5}	2.4	11	127(25)	–	–	–	4
$6_1 \rightarrow 6_0$	E	165 678.649^W	61.9	2.29×10^{-5}	2.8	13	312(31)	–	–	–	6
$7_1 \rightarrow 7_0$	E	166 169.098^W	78.2	2.28×10^{-5}	3.2	15	102(23)	–	–	–	4
$3_2 \rightarrow 2_1$	E	170 060.592^W	28.3	2.55×10^{-5}	1.6	7	275(53)	–	–	–	7
$1_1 \rightarrow 2_0$	A	205 791.270^F	16.8	6.28×10^{-5}	0.9	3	47(16)	10.3(0.4)	2.5(0.7)	18	2
$4_2 \rightarrow 3_1$	E	218 440.063^F	37.6	4.69×10^{-5}	1.7	9	180(10)	10.7(0.1)	1.5(0.1)	113	15
$8_{-1} \rightarrow 7_0$	E	229 758.756^F	81.2	4.19×10^{-5}	2.5	17	110(14)	10.7(0.1)	1.5(0.1)	69	5
$5_1 \rightarrow 4_1$	A	239 746.219^F	49.1	5.66×10^{-5}	4.8	11	74(14)	10.4(0.1)	1.4(0.1)	53	3
$5_0 \rightarrow 4_0$	E	241 700.159^F	40.0	6.04×10^{-5}	5.0	11	251(21)	10.8(0.1)	2.6(0.3)	90	7
$5_{-1} \rightarrow 4_{-1}$	E	241 767.234^F	32.5	5.81×10^{-5}	4.8	11	357(33)	10.4(0.2)	1.9(0.1)	224	15

Table B.10. continued.

Transition	Sym.*	Frequency	E_u/k	A_{ul}	S_{ul}	g_u	$\int T_{MB}\,dv$	v_{LSR}	Δv	T_{MB}	S/N
$(J_K)_u \rightarrow (J_K)_l$		[MHz]	[K]	[s^{-1}]			[mK km s^{-1}]	[km s^{-1}]	[km s^{-1}]	[mK]	
$5_0 \rightarrow 4_0$	A	241 791.352^F	34.8	6.05×10^{-5}	5.0	11	646(43)	10.5(0.2)	2.2(0.2)	273	27
$5_{-4} \rightarrow 4_{-4}$	E	241 813.255^F	114.8	2.18×10^{-5}	1.8	11	38(13)	10.7(0.2)	1.2(0.6)	28	2
$5_1 \rightarrow 4_1$	E	241 879.025^F	48.0	5.96×10^{-5}	5.0	11	205(25)	10.5(0.3)	3.3(0.6)	56	7
$5_{-2} \rightarrow 4_{-2}$	E	241 904.147^F	52.8	5.09×10^{-5}	4.2	11	⟩ 179(21)	10.5(0.1)	2.4(0.3)	67	7
$5_2 \rightarrow 4_2$	E	241 904.643^F	49.2	5.03×10^{-5}	4.2	11					
$5_{-1} \rightarrow 4_{-1}$	A	243 915.788^F	49.7	5.97×10^{-5}	4.8	11	72(13)	10.8(0.1)	0.7(0.2)	99	7
$2_1 \rightarrow 1_0$	E	261 805.675^F	20.1	5.57×10^{-5}	0.7	5	143(10)	10.7(0.1)	1.5(0.1)	89	7
$5_2 \rightarrow 4_1$	E	266 838.148^F	49.2	7.74×10^{-5}	1.9	11	225(12)	10.7(0.1)	1.7(0.1)	124	10
$9_{-1} \rightarrow 8_0$	E	278 304.512^F	102.1	7.69×10^{-5}	2.9	19	96(9)	10.7(0.1)	0.9(0.2)	100	10
$6_1 \rightarrow 5_1$	A	287 670.767^F	62.9	1.01×10^{-4}	5.9	13	80(9)	10.8(0.2)	1.8(0.1)	42	3
$6_{-1} \rightarrow 5_{-1}$	A	292 672.889^F	63.7	1.06×10^{-4}	5.9	13	82(23)	10.8(0.1)	0.9(0.2)	90	10
$3_0 \rightarrow 2_{-1}$	E	302 369.773^F	19.2	4.66×10^{-5}	0.5	7	34(14)	10.0(0.1)	0.4(0.2)	84	3
$1_{-1} \rightarrow 1_0$	A	303 366.921^F	16.9	2.26×10^{-4}	1.0	3	171(14)	10.5(0.1)	1.8(0.1)	89	5
$2_{-1} \rightarrow 2_0$	A	304 208.348^F	21.6	2.12×10^{-4}	1.6	5	228(14)	10.3(0.1)	1.6(0.1)	134	7
$7_0 \rightarrow 6_0$	E	338 124.488^F	70.2	1.70×10^{-4}	7.0	15	174(53)	10.5(0.2)	1.6(0.6)	101	3
$7_{-1} \rightarrow 6_{-1}$	E	338 344.588^F	62.7	1.67×10^{-4}	6.9	15	260(64)	10.7(0.1)	1.5(0.2)	235	11
$7_0 \rightarrow 6_0$	A	338 408.698^F	65.0	1.70×10^{-4}	7.0	15	440(69)	10.7(0.1)	1.6(0.1)	259	12
$7_3 \rightarrow 6_3$	E	338 583.216^F	104.8	1.39×10^{-4}	5.8	15	59(20)	11.0(0.1)	0.4(0.1)	133	3
$7_2 \rightarrow 6_2$	E	338 721.693^F	79.4	1.55×10^{-4}	6.4	15	⟩ 161(22)	10.5(0.1)	1.3(0.1)	117	3
$7_{-2} \rightarrow 6_{-2}$	E	338 722.898^F	83.0	1.57×10^{-4}	6.5	15					

Notes. Frequencies, E_u/k, A_{ul}, S_{ul}, and g_u from JPL catalogue.

Table B.11. Line parameters of CH_3CHO.

Transition	Sym.*	Frequency	E_u/k	A_{ul}	S_{ul}	g_u	$\int T_{MB}\,dv$	v_{LSR}	Δv	T_{MB}	S/N
$(J_{K_a,K_c})_u \rightarrow (J_{K_a,K_c})_l$		[MHz]	[K]	[s^{-1}]			[mK km s^{-1}]	[km s^{-1}]	[km s^{-1}]	[mK]	
$5_{1,5} \rightarrow 4_{1,4}$	A	93 580.909^F	15.7	2.63×10^{-5}	5.2	11	60(6)	10.4(0.1)	2.7(0.3)	21	6
$5_{1,5} \rightarrow 4_{1,4}$	E	93 595.235^F	15.7	2.63×10^{-5}	5.2	11	51(7)	10.8(0.2)	2.3(0.4)	21	6
$5_{0,5} \rightarrow 4_{0,4}$	E	95 947.437^F	13.8	2.96×10^{-5}	5.4	11	29(6)	10.7(0.3)	2.0(0.4)	13	3
$5_{0,5} \rightarrow 4_{0,4}$	A	95 963.459^F	13.8	2.95×10^{-5}	5.4	11	54(13)	10.7(0.2)	2.0(0.5)	25	3
$5_{1,4} \rightarrow 4_{1,3}$	E	98 863.314^F	16.5	3.10×10^{-5}	5.2	11	79(6)	11.1(0.3)	2.9(0.5)	26	3
$5_{1,4} \rightarrow 4_{1,3}$	A	98 900.944^F	16.5	3.11×10^{-5}	5.2	11	63(10)	11.1(0.1)	1.6(0.3)	38	7
$6_{1,6} \rightarrow 5_{1,5}$	A	112 248.716^F	21.1	4.67×10^{-5}	6.3	13	57(10)	10.7(0.2)	2.0(0.3)	27	5
$6_{1,6} \rightarrow 5_{1,5}$	E	112 254.508^F	21.1	4.67×10^{-5}	6.3	13	46(11)	11.2(0.2)	1.9(0.5)	23	4
$6_{0,6} \rightarrow 5_{0,5}$	E	114 940.175^F	19.4	5.16×10^{-5}	6.5	13	95(18)	11.0(0.2)	2.2(0.5)	40	4
$6_{0,6} \rightarrow 5_{0,5}$	A	114 959.902^F	19.4	5.15×10^{-5}	6.5	13	106(15)	10.6(0.1)	2.0(0.3)	49	5
$7_{1,7} \rightarrow 6_{1,6}$	A	130 891.821^W	27.4	7.54×10^{-5}	7.4	15	⟩ 135(44)	–	–	–	4
$7_{1,7} \rightarrow 6_{1,6}$	E	130 892.749^W	27.4	7.55×10^{-5}	7.4	15					

Table B.11. continued.

Transition	Sym.*	Frequency	E_u/k	A_{ul}	S_{ul}	g_u	$\int T_{MB} dv$	v_{LSR}	Δv	T_{MB}	S/N
$(J_{K_a,K_c})_u \rightarrow (J_{K_a,K_c})_l$		[MHz]	[K]	[s^{-1}]			[mK km s^{-1}]	[km s^{-1}]	[km s^{-1}]	[mK]	
$7_{1,6} \rightarrow 6_{1,5}$	A	138 319.628^W	28.8	8.90×10^{-5}	7.4	15	166(62)	–	–	–	3
$8_{1,8} \rightarrow 7_{1,7}$	E	149 505.128^W	34.6	1.14×10^{-4}	8.5	17	193(96)	–	–	–	2
$8_{1,8} \rightarrow 7_{1,7}$	A	149 507.462^W	34.6	1.14×10^{-4}	8.5	17					
$8_{0,8} \rightarrow 7_{0,7}$	E	152 607.614^W	33.1	1.23×10^{-4}	8.6	17	184(74)	–	–	–	4
$8_{1,7} \rightarrow 7_{1,6}$	E	157 937.697^W	36.4	1.34×10^{-4}	8.5	17	86(21)	–	–	–	4
$8_{1,7} \rightarrow 7_{1,6}$	A	157 974.590^W	36.4	1.34×10^{-4}	8.5	17	105(24)	–	–	–	6
$9_{1,9} \rightarrow 8_{1,8}$	E	168 088.618^W	42.6	1.64×10^{-4}	9.6	19	98(36)	–	–	–	3
$9_{1,9} \rightarrow 8_{1,8}$	A	168 093.444^W	42.7	1.64×10^{-4}	9.6	19					
$9_{0,9} \rightarrow 8_{0,8}$	A	171 296.985^W	41.3	1.75×10^{-4}	9.7	19	158(92)	–	–	–	2
$11_{1,11} \rightarrow 10_{1,10}$	E	205 161.898^F	61.4	3.02×10^{-4}	11.7	23	74(10)	10.6(0.2)	2.4(0.3)	29	4
$11_{1,11} \rightarrow 10_{1,10}$	A	205 170.686^{F,B}	61.5	3.01×10^{-4}	11.7	23	–	–	–	–	–
$11_{0,11} \rightarrow 10_{0,10}$	A	208 267.045^F	60.4	3.17×10^{-4}	11.8	23	62(9)	10.6(0.1)	1.8(0.3)	33	5
$11_{1,10} \rightarrow 10_{1,9}$	E	216 581.930^F	64.8	3.55×10^{-4}	11.7	23	47(10)	10.7(0.2)	1.4(0.5)	32	5
$11_{1,10} \rightarrow 10_{1,9}$	A	216 630.234^F	64.8	3.55×10^{-4}	11.7	23	53(7)	10.7(0.1)	1.5(0.2)	33	5
$12_{1,12} \rightarrow 11_{1,11}$	E	223 650.093^F	72.2	3.92×10^{-4}	12.8	25	68(9)	10.8(0.1)	1.9(0.3)	34	6
$12_{1,12} \rightarrow 11_{1,11}$	A	223 660.603^F	72.2	3.92×10^{-4}	12.8	25	58(11)	10.7(0.2)	2.2(0.5)	24	4
$12_{0,12} \rightarrow 11_{0,11}$	E	226 551.622^F	71.3	4.10×10^{-4}	12.9	25	114(6)	10.5(0.3)	2.5(0.5)	43	6
$12_{0,12} \rightarrow 11_{0,11}$	A	226 592.725^F	71.3	4.10×10^{-4}	12.9	25	54(15)	11.4(0.1)	1.0(0.4)	50	4
$12_{1,11} \rightarrow 11_{1,10}$	E	235 996.212^F	76.1	4.61×10^{-4}	12.8	25	77(23)	10.8(0.3)	2.0(0.8)	36	3
$12_{1,11} \rightarrow 11_{1,10}$	A	236 049.131^F	76.1	4.61×10^{-4}	12.8	25	39(15)	10.8(0.2)	1.0(0.5)	38	3
$13_{1,13} \rightarrow 12_{1,12}$	A	242 118.136^F	83.8	5.00×10^{-4}	13.9	27	43(17)	10.0(0.5)	2.5(1.3)	16	2
$13_{0,13} \rightarrow 12_{0,12}$	A	244 832.176^F	83.1	5.18×10^{-4}	13.9	27	48(10)	11.5(0.1)	1.2(0.3)	39	3
$13_{1,12} \rightarrow 12_{1,11}$	E	255 326.968^F	88.4	5.86×10^{-4}	13.9	27	65(13)	10.9(0.2)	2.0(0.5)	30	5
$13_{1,12} \rightarrow 12_{1,11}$	A	255 384.754^F	88.4	5.86×10^{-4}	13.9	27	67(10)	10.6(0.1)	1.8(0.3)	34	6
$14_{0,14} \rightarrow 13_{0,13}$	E	262 960.097^F	95.7	6.44×10^{-4}	15.0	29	32(7)	10.5(0.2)	1.3(0.3)	23	4
$14_{1,13} \rightarrow 13_{1,12}$	E	274 563.412^F	101.5	7.31×10^{-4}	15.0	29	38(11)	10.9(0.2)	1.0(0.3)	35	2
$15_{1,15} \rightarrow 14_{1,14}$	A	278 939.438^F	109.7	7.69×10^{-4}	16.1	31	22(7)	10.5(0.2)	1.0(0.4)	23	3
$15_{0,15} \rightarrow 14_{0,14}$	A	281 126.944^F	109.2	7.88×10^{-4}	16.1	31	29(11)	10.7(0.3)	1.4(0.5)	19	2

Notes. ^{B} Blended with CF^+ $2 \rightarrow 1$. Frequencies, E_u/k, A_{ul}, S_{ul}, and g_u from JPL catalogue.